Article

Assessment of a Mid-Fidelity Numerical Approach for the Investigation of Tiltrotor Aerodynamics

Alex Zanotti *, **Alberto Savino**, **Michele Palazzi**, **Matteo Tugnoli** and **Vincenzo Muscarello**

Politecnico di Milano, Dipartimento di Scienze e Tecnologie Aerospaziali, Via La Masa 34, 20156 Milan, Italy; alberto.savino@polimi.it (A.S.); michele.palazzi@mail.polimi.it (M.P.); matteo.tugnoli@polimi.it (M.T.); vincenzo.muscarello@polimi.it (V.M.)
* Correspondence: alex.zanotti@polimi.it

Abstract: The study of the complex aerodynamics that characterise tiltrotors represents a challenge for computational fluid dynamics tools. URANS numerical solvers are typically used to explore the aerodynamic features that characterise the different flight conditions of these aircraft, but their computational cost limits their applications to a few vehicle configurations. The present work explores the capabilities of a new mid-fidelity aerodynamic code that is based on the vortex particle method, DUST, to investigate the performance and flow physics of tiltrotors. With this aim, numerical simulations were performed in DUST while considering XV-15 tiltrotor configurations with increasing complexity. The study started with the investigation of a simpler configuration made up of a single wing and a proprotor. Subsequently, the full aircraft was studied in steady-level flights and its major operating flight conditions were explored—i.e., hover, conversion phase, and cruise. A thorough assessment of the code capabilities was performed by the comparison of the numerical results with high-fidelity Computational Fluid Dynamics (CFD) data. This thorough comparison showed that the mid-fidelity numerical approach implemented in DUST is suitable for capturing the flow physics related to the complex aerodynamic interactions between the proprotors and the wing along with the entire flight envelope of the tiltrotor. Moreover, a good representation of the aerodynamic performance of the vehicle was obtained, particularly for the flight conditions that are characterised by limited flow separations. The good accuracy obtained for both the performance and flow physics, combined with the relatively lower computational costs required by the mid-fidelity solver with respect to the URANS simulations, indicates that DUST could be considered a valuable tool for use in the preliminary design of novel tiltrotor configurations.

Keywords: rotorcraft aerodynamics; tiltrotor; computational fluid dynamics; vortex particle method

1. Introduction

Tiltrotors combine the speed and range of a conventional fixed-wing aircraft with the vertical take-off and landing capabilities of helicopters. Their architecture is typically characterised by two powered rotors that are mounted on tilting nacelles located at the outer portion of the wing. The flight mission of tiltrotors involves different vehicle configurations characterised by several relative angles between rotor nacelles and wing. Indeed, tiltrotors take off as a helicopter with the rotors tilted vertically (see Figure 1a) and they turn the rotors forward in cruise conditions to behave as a fixed wing airplane (see Figure 1d). In the conversion phase between take-off and cruise flight conditions, the aircraft rotates the rotors providing different tilting angles between the rotors and wing axis (see Figure 1b,c). Consequently, tiltrotor aerodynamics are characterised by complex interactions between the rotor wake and wing that are peculiar of the different attitudes experienced by the vehicles during their flight mission. Several experiments have been conducted to investigate rotor–wing interactions, from the early stages of the JVX program [1,2] to the present day [3,4].

Recent advances in the field of high-performance computing favoured the use of high-fidelity Computational Fluid Dynamics (CFD) for a thorough investigation of the

complex aerodynamic interactions that characterise tiltrotor architectures. Indeed, several numerical works employing the use of high-fidelity Navier–Stokes equations solvers for the study of tiltrotor aerodynamics can be found in the literature. Examples of computational studies of tiltrotor aerodynamics are the works by Meakin [5], Potsdam and Strawn [6], and Wissink et al. [7], where hover configurations were simulated while using different implementations of the Navier–Stokes equations.

(**a**) Bell XV-15

(**b**) Leonardo AW-609

(**c**) Bell Boeing V-22

(**d**) Bell XV-3

Figure 1. Examples of tiltrotor aircraft in different flight conditions: (**a**) Bell XV-15 in hover [8]; (**b**) Leonardo AW-609, in early conversion phase https://www.leonardocompany.com/it/products/aw609; (**c**) Bell Boeing V-22 in advanced conversion phase, http://www.military-today.com/helicopters/; and, (**d**) Bell XV-3 in cruise [8].

Moreover, several high-fidelity CFD codes, such as elsA [9] by ONERA, FLOWer [10] by DLR and Airbus Helicopters Deutschland, HBM3 by the University of Glasgow [11], and ROSITA [12] by Politecnico di Milano, were developed in Europe for rotorcraft application studies. These codes, based on the block-structured grid, finite volume, and Chimera approaches for the simulation of rotating bodies, were used and compared for the study of the aerodynamics of the tiltwing aircraft ERICA [13,14] and, in particular, within the European project NICETRIP [15]. In the recent literature, several numerical works were carried out to simulate the aerodynamics of the XV-15 tiltrotor aircraft using high-fidelity CFD tools. Indeed, in these works, Lim and Tran et al. [16–19] investigated the main aerodynamic interactions between the rotor and the wing of the XV-15 tiltrotor.

Nevertheless, time-accurate URANS simulations of tiltrotor aircraft configurations still require a huge computational effort. Thus, high-fidelity CFD tools are usually employed for the detailed study of a limited number of tiltrotor configurations in steady-state conditions, as done in [16,17]. Mid-fidelity aerodynamic solvers that are based on unsteady panel methods are considered of great interest in the field of rotorcraft simulations. As a matter of fact, the limited computational effort that is required by these numerical tools enables one to perform the large number of aerodynamic simulations required for the preliminary design of novel rotary-wing vehicles. To cite few examples of numerical works involving the use of unsteady panel methods for rotorcraft applications, the University of Roma Tre developed a direct panel method based on a novel boundary integral formulation for the velocity potential that was used both for the investigation of blade vortex interaction of helicopter rotors [20] and for the study of wing-proprotor aerodynamic interaction of tiltrotors [21]. More recently, DLR developed an unsteady panel, free-wake code that was used for the aerodynamic study of a complex rotorcraft configurations, such as the Airbus RACER compound helicopter [22]. In particular, recent works used the vortex particle method (VPM) [23,24] for wake modelling, showing a quite accurate representation of the aerodynamic interactions among several bodies that are typical of complex rotorcraft configurations. To cite few examples, Lu et al. [25] developed a method for the optimisation of the aerodynamic layout of a helicopter using an aerodynamic model based on viscous VPM combined with an unsteady panel hybrid method to simulate the interactions between the various components of a helicopter. The National Technical University of Athens developed the GENeral Unsteady Vortex Particle (GENUVP) software based on a panel method coupled with a VPM solver that was used for both aerodynamic and aeroacoustic simulations of rotorcraft [26]. Alvarez and Ning investigated multi-rotors configurations using a VPM-based code [27], showing good agreement with experimental data. Moreover, Tan et al. used a vortex-based approach coupled with a viscous boundary model to investigate the complex rotorcraft-to-rotorcraft interference problems that occur during shipboard operations—i.e., the flow field and unsteady airloads of a tiltrotor affected by the wake of an upwind tandem rotor [28].

In recent years, a new flexible mid-fidelity computational tool, called DUST (www.dust-project.org), was developed as the result of a collaboration between Politecnico di Milano and A^3 by Airbus LLC, aiming to obtain a fast and reliable numerical tool for the aerodynamic simulation of complex rotorcraft configurations, such as eVTOLs aircraft. DUST is an open source code that was developed under an MIT license, simultaneously involving different aerodynamic modelling techniques, such as thick surface panels, thin vortex lattices, and lifting lines for solid bodies, while vortex particles were used for wake modelling. In particular, the implemented vortex particle model for wakes provides a stable Lagrangian description of the free vorticity field in the flow, which is suitable for numerical simulations with strong aerodynamic interactions. Indeed, for instance, DUST was used to simulate the aerodynamics of the full Vahana vehicle that was developed by A^3 by Airbus LLC [29] characterised by two rows of four rotors in a tandem configuration, showing a quite good agreement with both the flight test data and high-fidelity CFD results [30]. Moreover, thanks to the low computational effort that is required by the code implementation, DUST was recently employed to perform a parametric study of the rotor-rotor aerodynamic interaction that characterises the cruise flight conditions of an eVTOL aircraft [31]. Consequently, DUST can be considered in a mature state to be used for the investigation of challenging rotorcraft configurations that are characterised by complex aerodynamic interactions between rotors and wings.

The present work aims to assess the accuracy of the mid-fidelity approach that was implemented in DUST for the simulation of tiltrotor aerodynamics with respect to CFD. In particular, numerical simulations were performed with DUST to show the ability of a mid-fidelity solver to capture the effects of the complex aerodynamic interactions between the rotor wake and the wing typical of the different stages of a tiltrotor flight mission. Indeed, the scope of the work is to investigate the suitability of a mid-fidelity solver for

the preliminary design of complex rotorcraft architectures, such as tiltrotors, which require a huge number of numerical simulations. In particular, the work was performed in the framework of the FORMOSA project, which aimed at the design of the novel wing movable surface system of the NextGen Civil Tiltrotor aircraft developed within the framework of the Clean Sky 2–H2020 Programme.

In the present paper, the results of the DUST simulations over a complete tiltrotor model in different flight conditions are compared with the results that were obtained using a numerical approach with a higher fidelity, such as URANS simulations. In particular, the test case considered in the present work is the XV-15 aircraft due to the accessible and comprehensive data available in the literature. Indeed, this vehicle was commonly considered as a reference to validate fluid dynamics code for tiltrotor applications, as achieved, for example, by Garcia et al. [32]. The numerical activity performed with DUST considered the steady-state conditions of the complete XV-15 tiltrotor aircraft in hover, conversion, and cruise conditions to be compared with the recent results that were obtained with the URANS CFD solver presented in the works by Tran et al. [16,17]. Hereafter, the results obtained from these reference works will be outlined as CFD results. The extensive assessment described in the present work clearly indicates the limits and robustness of a mid-fidelity numerical approach with respect to higher-fidelity CFD solvers for the investigation of the main interacting flow features that characterise tiltrotor aerodynamics. Moreover, the results that are presented in this work indicate that mid-fidelity solvers can be considered to be valuable tools for engineers for use in the preliminary phase of the design process of unconventional VTOL aircraft. Consequently, the results presented in this work represent a thorough assessment of a novel milestone in the computational fluid dynamics tools used by the aerospace community for the development and study of the aerodynamics of novel aircraft architectures. The paper is organised, as follows. Section 2 outlines the numerical approach implemented in DUST. Section 3 provides the description of the numerical models implemented for the study of the XV-15 tiltrotor aerodynamics, along with the validation of the parameters used for DUST simulations by means of comparison with the experimental data available for the single rotor in hover. Section 4 presents the main results that were obtained in DUST compared with the CFD simulation results available in the literature, starting from a simplified configuration made up of a single wing and rotor to the complete tiltrotor aircraft in different flight conditions. Conclusions are drawn in Section 5.

2. Numerical Approach Implemented in DUST

DUST is an open source software that was built with the object-oriented paradigms of the latest FORTRAN standards aiming to solve complex aerodynamics problems with a flexible and reliable approach. The mathematical formulation of the problem relies on Helmholtz's decomposition of the velocity field $\vec{u} = \vec{u}_\varphi + \vec{u}_\psi$, with $\vec{u}_\varphi$ and $\vec{u}_\psi$ being the irrotational and solenoidal contributions, respectively, to recast the aerodynamic problem as a combination of a boundary value problem for the potential part of the velocity and a mixed panels-vortex particles model of the free vorticity in the flow. The solution is advanced in time using a time-stepping algorithm that alternates the solution of a three-dimensional boundary element method for $\vec{u}_\varphi$ and the Lagrangian evolution in time of the rotational part of the velocity $\vec{u}_\psi$. Only the surface mesh of the model is required and different aerodynamic elements allow for different levels of fidelity in the model, ranging from lifting line elements to zero-thickness lifting surfaces and surface panels. A piecewise-uniform distribution of doublets and sources is associated with surface panels, according to a Morino-like formulation for the velocity potential [33]. Thin lifting bodies can also be modelled as zero-thickness surfaces of vortex lattice elements, for which a velocity-based non-penetration condition is assigned. The mixed potential-velocity formulation of the boundary element problem results in a linear system whose unknown is the intensity of the doublet distribution on the surface panels and the equivalent doublet intensity of the vortex lattice elements.

One-dimensional lifting line elements are used for a proper modelling of lifting bodies with a high aspect ratio, such as rotor blades. These elements naturally represent viscous effects, since they rely on the tabulated aerodynamic lift, drag, and moment coefficients of two-dimensional sections as functions of the relative velocity direction and magnitude. Each lifting line element is modelled as a vortex ring that is composed by the lifting line segment along with its trailing vortices. The last line vortex is released in the wake aligned with the spanwise direction. The intensity Γ of this vortex ring and, thus, of the lifting line, is determined through a fixed point algorithm solving a nonlinear problem, connecting the intensity of the lifting line elements with the tabulated aerodynamic coefficients of the lifting sections. Both a loosely coupled Γ method [34] and a α method [35] solver are available in the DUST formulation. An iterative procedure is used to solve the nonlinear problem of computing the loads on lifting lines, while taking into account their mutual interference, using the unsteady formulation of the Kutta–Joukowski theorem to retrieve the circulations of the elements from their lift.

A more detailed description of the whole numerical approach implemented in DUST can be found in [30,36]. In the following, a brief description of the core of the code that is represented by the implemented VPM is provided.

Vortex Particle Method

The wake shed from the trailing edges of lifting bodies is modeled as a panel wake, which shares the same spatial discretisation that is used to model the lifting bodies and the same formulation as vortex lattice elements in terms of geometry and singularity distribution. When advected downstream, the panel wake is converted into vortex particles in order to obtain a more robust wake formulation that is suitable for the representation of the interactional aerodynamics of both rotorcraft and complex aircraft configurations. The vortex particles method (VPM) [23,24] is a Lagrangian grid-free method describing the wake evolution through the rotational component of the velocity field $\vec{u}_\psi$ by means of the material vortex particles used to obtain the approximated vorticity field—namely:

$$\vec{\omega}^h(\vec{r}, t) = \sum_{p=1}^{N_p} \vec{\alpha}_p(t) \zeta\left(\vec{r} - \vec{r}_p(t); R_p\right) , \qquad (1)$$

where $\vec{r}_p(t)$ is the position, $\vec{\alpha}_p(t)$ is the intensity, and R_p is the radius of the p-th vortex particle, while $\zeta(r)$ is the cut-off function while considering the vorticity distribution that is induced by each particle. By substituting (1) in the equation of the dynamics of vorticity,

$$\frac{D\vec{\omega}}{Dt} = \vec{\omega} \cdot \nabla \vec{u} + \nu \nabla^2 \vec{\omega} , \qquad (2)$$

the dynamical equations for the intensity $\vec{\alpha}_p(t)$ and position $\vec{r}_p(t)$ of all the material vortex particles to be integrated in time can be obtained, as follows:

$$\begin{cases} \dfrac{d\vec{\alpha}_p}{dt} = \vec{\alpha}_p \cdot \nabla \vec{u}(\vec{r}_p(t), t) + \nu \text{ " } \nabla^2 \vec{\alpha}_p \text{ "} \\ \dfrac{d\vec{r}_p}{dt} = \vec{u}(\vec{r}_p(t), t) . \end{cases} \qquad (3)$$

The viscosity diffusion term " $\nabla^2\vec{\alpha}_p$ " is calculated while using the particle strength exchange (PSE) method, which approximates the Laplacian operator acting on the vorticity field with an integral operator, as reported in [24].

The mathematical formulation used in the solver relies on the Helmholtz decomposition of the velocity field $\vec{u} = \vec{u}_\varphi + \vec{u}_\psi$. The irrotational velocity $\vec{u}_\varphi$ is induced by the free stream velocity, by the singularity distributions of sources and doublets on the body surface, and by the wake panels, while the rotational velocity $\vec{u}_\psi$ is induced by the vortex particles. Moreover, the solenoidal constraint on the rotational velocity, $\nabla \cdot \vec{u}_\psi = 0$, is used

in order to define the vector potential $\vec{\psi}$, s.t. $\vec{u}_\psi = \vec{\nabla} \times \vec{\psi}$. Consequently, Poisson's equation is obtained for $\vec{\psi}$:

$$-\nabla^2 \vec{\psi} = \vec{\omega} \, , \tag{4}$$

where we consider the gauge condition $\nabla \cdot \vec{\psi} = 0$, the vorticity field definition $\vec{\omega} = \nabla \times \vec{u}$, and the vector identity $\nabla \times \vec{u}_\varphi = \nabla \times \nabla \varphi = 0$. Poisson's equation solution (4) reads:

$$\vec{\psi}(\vec{r}, t) = \int_{V_0} G(\vec{r}, \vec{r}_0) \, \vec{\omega}(\vec{r}_0, t) dV_0 \, , \tag{5}$$

$$\vec{u}_\psi(\vec{r}, t) = \int_{V_0} \vec{K}(\vec{r}, \vec{r}_0) \times \vec{\omega}(\vec{r}_0, t) dV_0 \tag{6}$$

where $G(\vec{r}, \vec{r}_0)$ is Green's function of the Laplace equation and $\vec{K}(\vec{r}, \vec{r}_0)$ represents its gradient with respect to the first argument.

Substituting the definition of the discretised vorticity field of the particles (1) into Equation (6), the contribution of velocity that is induced by the particles can be obtained, as follows:

$$\vec{u}_\psi^h(\vec{r}, t) = \sum_{p=1}^{N_p} \vec{K}^h(\vec{r} - \vec{r}_p(t)) \times \vec{\alpha}_p(t) \, . \tag{7}$$

The discrete kernel $\vec{K}^h(\vec{r} - \vec{r}_p(t))$ must be consistent with the selected cutoff function ζ. The cutoff function in the singular vortex particle method is a Dirac delta function, and the Biot–Savart kernel is retrieved. In the DUST implementation, the selected cutoff function ζ leads to the Rosenhead–Moore kernel:

$$\vec{K}^h(\vec{x}, \vec{y}) = -\frac{1}{4\pi} \frac{\vec{x} - \vec{y}}{(|\vec{x} - \vec{y}|^2 + R_v^2)^{3/2}} \, , \tag{8}$$

This is a regular kernel fitting naturally in the Cartesian fast multipole method (FMM) [37,38]. The induced rotational velocity $\vec{u}_\psi$ has to be accounted for in the material objects' convection and in the right-hand side of the linear system of equations for the potential velocity. Moreover, the velocity field gradient is calculated to evaluate the vortex stretching-tilting term with the FMM. Indeed, this term is a function of both the vortex intensities and the particle distance in particle-to-particle interactions [24].

3. Numerical Models

3.1. Proprotor Numerical Model

The numerical activity started with the modelling of the single proprotor of the XV-15 tiltrotor, because, owing to the availability of the experimental results concerning this configuration in hover, this test case was used to validate DUST simulation parameters that are therefore used for the analysis of the full aircraft. With this aim, the results from the experimental activity conducted on the full-scale XV-15 single proprotor equipped with metal blades in hover were considered for validation. The experimental campaign took place at the Outdoor Aerodynamic Research Facility (OARF), as described in the work by Felker et al. [39]. The experimental data are collected in the work by Bartie et al. [40], reporting an error in the measurements of the collective pitch of 4°. Therefore, the data that are presented in the following have been corrected accordingly. Harris [41] reported the whole set of experimental data measured in hover in 2017 in a more modern and legible document.

The blade of the XV-15 proprotor was modelled according to the geometry described in [39,42]. Table 1 reports the main characteristics of the proprotor that are used in the experiments, while Table 2 reports the airfoils distribution used for the blade geometry.

Table 1. XV-15 full-scale proprotor characteristics.

Number of Blades	3
Radius [m]	3.81
Disc Area [m^2]	45.6
Solidity	0.089
Precone angle [°]	2.5
Overall twist [°]	−40.9
Hover RPM	589

Table 2. Blade airfoils distribution for the XV-15 full-scale proprotor [39].

r/R	Airfoil
0.09	NACA 64-935 a = 0.3
0.17	NACA 64-528
0.51	NACA 64-118
0.80	NACA 64-(1.5)12
1.00	NACA 64-208 a = 0.3

A numerical model of the full-scale XV-15 right-hand proprotor was built for DUST simulations while considering the airfoil geometry, chord, twist, sweep, and dihedral distributions reported in [39]. Each of the three blades was modelled using lifting line elements that included the viscosity contributions to aerodynamic loads through tabulated sectional aerodynamic data. The tabulated data of the blade airfoils were computed by XFOIL simulations [43], before the stall angle of attack. The two-dimensional aerodynamic load curves were corrected to be extended to the ±180° range of angles of attack using the methods that are described in [44,45].

Time and spatial dependence studies were performed for the single proprotor test case in hover, with the blade collective pitch angle set to $\theta = 11°$. This value was selected because it is similar to the blade collective pitch angle of the full-vehicle in hover condition, as reported in [46]. Thus, numerical simulations were performed with DUST, fixing the spatial discretisation to 20 lifting line elements for each blade and changing the time discretisation of the simulation between 20 and 80 time steps throughout a length of ten rotor revolutions (N_{rev}). This time dependence analysis shows that the average thrust and torque coefficients that were obtained over the last two revolutions change negligibly with a time discretisation finer than 9° for the blade azimuthal angle for each rotor revolution (40 time steps). Therefore, a spatial dependence analysis was performed, fixing the time discretisation of the simulations to 40 time steps for the rotor revolution and changing the number of lifting line elements between 20 and 70 to model each of the three blades. The simulation results show negligible variations in the thrust and torque coefficients, increasing the spatial discretisation over 35 lifting line elements. Consequently, the time and spatial discretisations that were outlined by the dependence analysis were used for the validation of the numerical model by comparison with the experiments. The complete description of the dependence studies is reported in [47].

Thus, simulations with DUST were performed for the XV-15 full-scale proprotor, reproducing the hover condition and the sweep of blade collective pitch angles reported in [39]. The numerical simulations were advanced in time with a discretisation of 9° of the blade azimuthal angle for each rotor revolution, while each blade was modelled using 35 lifting line elements. Figure 2a shows the time histories of the single proprotor thrust coefficient C_T in hover throughout ten rotor revolutions for some of the selected blade pitch angles (θ) that were considered by the DUST simulations. The curves' behaviour shows that after three rotor revolutions, the computed thrust coefficients reach a steady value for all the considered blade collective pitch angles. This result confirms that a number of ten rotor revolutions can be considered enough to reproduce a fully developed wake of the proprotor and obtain converged values for the proprotor aerodynamic performance.
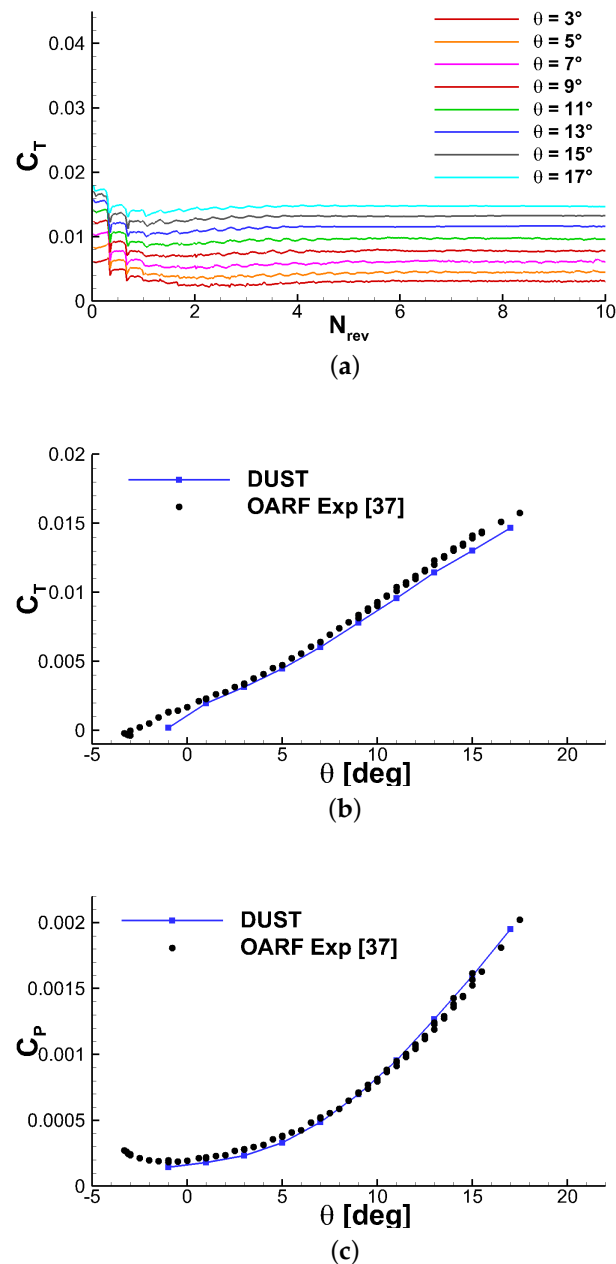
(a)

(b)

(c)

Figure 2. Comparison of the results obtained for the XV-15 full-scale single proprotor in hover. (**a**) Time histories of the thrust coefficient C_T calculated by DUST as a function of the number of rotor revolutions N_{rev}; (**b**,**c**) comparison of the DUST simulations results with experimental data from [39].

Figure 2b,c show the comparison of the DUST simulation results with the experimental data from [39]. The results that were reported for the DUST simulations were obtained by averaging the C_T and C_P over the last two rotor revolutions. A quite good agreement between the DUST simulation results and the experiments was found for both the thrust and power coefficients in the whole range of collective pitch angles considered. This comparison confirms that the parameters used to build the numerical model of the XV-15 proprotor are suitable to reproduce the aerodynamic performance accurately. Therefore, the numerical model parameters identified in this preliminary study were used for the following simulations.

3.2. Wing-Proprotor Numerical Model

In order to better evaluate the capabilities of DUST in capturing the main aerodynamic features related to rotor/wing interaction for tiltrotor configurations, simulations were performed over a simplified numerical model made by the XV-15 proprotor described in Section 3.1 and a simplified rectangular wing, as suggested by the numerical work by Lim [18]. The numerical model of the wing was built using a symmetric NACA 0023 airfoil at incidence $\alpha = 5°$ instead of the cambered NACA 64A223 airfoil used for the XV-15 tiltrotor, as in the work by Lim [18]. No sweep or dihedral was introduced to the wing model, while the full span of 9.8 m (386 inches) and the chord of 1.6 m (63 inches) were considered. The wing was modelled with surface panels, while the same numerical model built by lifting line elements for proprotor blades was kept for this configuration. The wake of both wing and proprotor was modelled by vortex particles. The goal of this activity was to provide a direct comparison between the DUST simulations and the CFD results that were obtained by Lim [18]. Thus, the cruise condition at 220 kts with the proprotor operating at 517 RPM was considered in this preliminary study. A spatial dependence study on the wing mesh was performed with DUST by running simulations of the single-wing model in cruise with different surface panel densities. In particular, simulations were performed fixing the spanwise discretisation to 102 surface panels and changing the chordwise discretisation between 100 and 300 surface panels. This dependence study, as reported in detail in [47], shows that the use of 300 surface panels for chordwise discretisation leads to an error of the computed lift of the wing below 2% of the value obtained by CFD [18]. Thus, the latter spatial discretisation was considered for the wing model as a fair compromise between accuracy and limited computational effort. Figure 3 shows a picture of the numerical model built for the wing-proprotor system, including the reference systems that are used to discuss the numerical results. The origin of the wing reference system $(X - Y - Z)$ is positioned at the midspan, while the origin of the radial coordinate (r) of the blades is positioned at the center of the rotor disk with the azimuthal angle of the blade ψ defined in Figure 3.
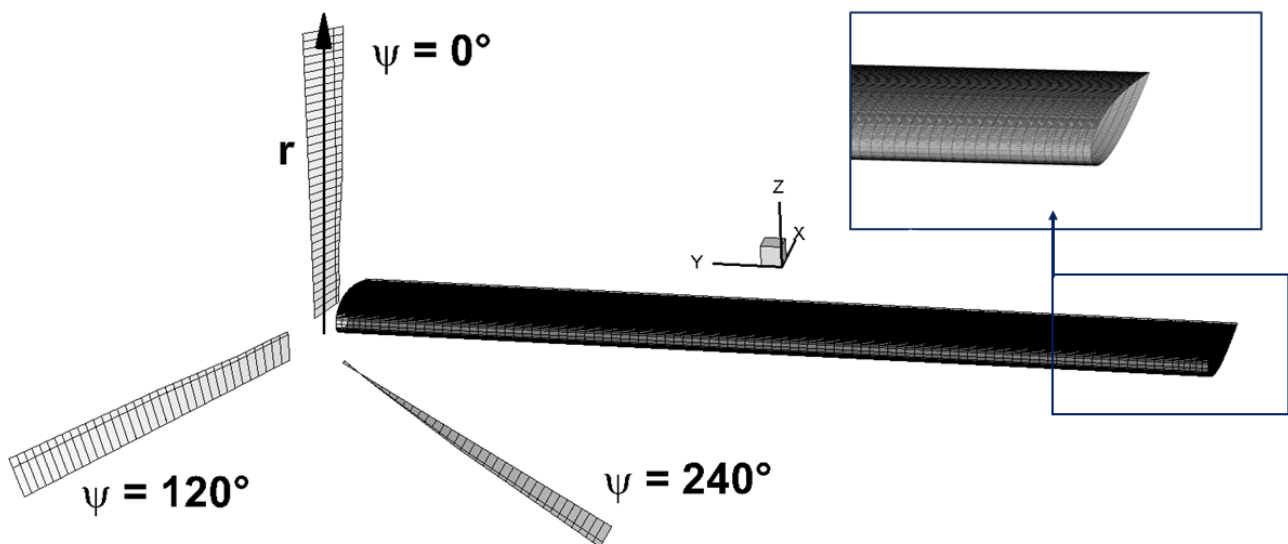

Figure 3. Layout of the numerical model of the wing/proprotor system; details of the surface mesh are shown in the zoomed inboard wing region.

A preliminary set of numerical simulations was performed with DUST for the single proprotor operating at 517 RPM for adjusting the collective pitch angle of the blades to trim the proprotor thrust to the value reported by CFD simulation in [18] for the same test case. Subsequently, the wing was added into the DUST simulations. This procedure allowed us to more clearly evaluate the aerodynamic interaction effects that were provided by the

wing. All of the DUST simulations were advanced in time using the time discretisation selected for the single proprotor test case—i.e., 40 time steps for rotor revolution for a total simulation length of ten rotor revolutions. The developed wake for the wing-proprotor simulation in cruise consisted of around 18 thousands vortex particles.

3.3. Full Vehicle Numerical Model

The full vehicle numerical model of the XV-15 tiltrotor was built while considering the full scale dimensions and components of the aircraft. The model included the fuselage with a length of 14.1 m, the horizontal and vertical tailplanes, the wing equipped with control surfaces (i.e., flap and flaperon), and the two proprotors with nacelles. Table 3 reports the main characteristics of the full vehicle geometry, including the airfoil series used to build the numerical model.

Table 3. Geometrical characteristics of the XV-15 full vehicle numerical model.

	Wing	**Horizontal Tail**	**Vertical Tail**
Airfoil	NACA 64A223	NACA 64015	NACA 0009
Span	9.8 m	3.91 m	2.34 m
Mean aerodynamic chord	1.60 m	1.20 m	1.13 m
Sweep ($c/4$)	$-6.5°$	$0°$	$31.6°$
Dihedral	$2.0°$	$0°$	-
Incidence	$3.0°$	$0°$	$0°$
	Flap	**Flaperon**	
Span along hinge line	1.30 m	2.40 m	
Chord/Wing chord	0.25	0.25	
Maximum deflection	$75°$	$47°$	

It must be remarked that the CFD works, selected as a reference for comparison with the DUST results, present some geometry inaccuracies with respect to the real aircraft. Indeed, during flight tests [48] the wing presented a Gurney flap, as reported in the last work by Tran and Lim [16]. This feature was not modelled in the work by Tran et al. [17] that was used hereafter for the comparison with DUST in hover and cruise conditions, while it was included in the latest simulations by the same authors [16] that were considered to be more accurate for the comparison in conversion mode.

For DUST simulations of the full vehicle, the authors decided to model the aircraft wing without a Gurney flap. Indeed, a possible attempt to model this feature with panel methods would provide a higher complexity and add potential inaccuracies to the numerical results that were not justified by the main scope of the work. Consequently, due to the difference in modelling between the numerical models built for the two CFD works used for reference, the overall lift of the aircraft will not be presented in the results discussion. On the other hand, the rotation of the vehicle wing control surfaces was correctly reproduced in the DUST simulations. Indeed, the last portion of the wing airfoil was tilted for the spanwise region of the flaps and flaperons, as indicated by the real aircraft geometry parameters that are presented in Table 3. The proprotor blades for the full vehicle simulations were modelled using lifting line elements using the spatial discretisation that is described in Section 3.1. All of the remaining components of the vehicle were modelled using surface panels. In particular, a total of 13758 elements were used to model the fuselage and tailplanes, 873 elements were used for each of the two nacelles, and each semi-span wing was modelled using 5400 elements. A picture of the mesh that was built for the full XV-15 tiltrotor is shown in Figure 4. No dependence studies were performed for the spatial discretisation of the full vehicle. Nevertheless, the meshing of the aircraft components surfaces was performed following best practices provided by a previous work performed with DUST on full aircraft configurations [30]. Moreover, the choice of the selected spatial and time discretisations for the full vehicle was dictated by the need to limit

the computational effort of the simulations. Indeed, the main aim of this work is to show the possible engineering application of a mid-fidelity numerical approach for aerodynamics for use in the preliminary design of novel tiltrotor configurations requiring a huge number of simulations. Thus, the DUST simulations for the full vehicle were advanced in time using the same time discretisation selected for the single proprotor test case—i.e., 40 time steps for rotor revolution for a total simulation length of ten rotor revolutions. The wake of all the lifting bodies, i.e., the wing, the vertical, and horizontal tailplanes was modelled by vortex particles. The developed wake for the full-vehicle simulations ranges from around 140 thousands vortex particles in hover flight condition to around 80 thousands vortex particles in cruise. The computational time for a single flight condition of the full vehicle was about 80 min. over a workstation that was equipped with a Intel® Core™ i9-9980XE processor running on a base frequency of 3.00 GHz, with 18 physical cores and 2 threads for each core.
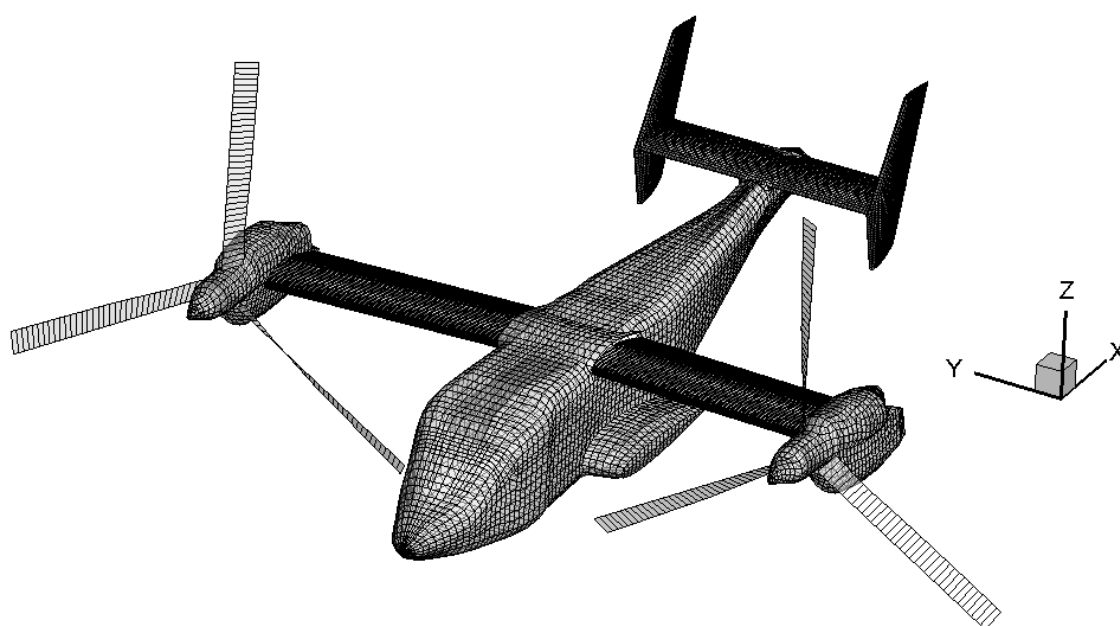
Figure 4. Layout of the numerical model of the full XV-15 tiltrotor.

In the present work, the DUST simulations analysed the different flight conditions that characterise the tiltrotor mission—i.e., hover, conversion, and cruise. In particular, the flight parameters that were investigated in the CFD works by Tran et al. [17] and by Tran and Lim [16] were reproduced in DUST simulations, as shown in Table 4. The main parameters of the aircraft are illustrated in the sketch of Figure 5.

Table 4. Parameters of the full XV-15 vehicle configurations considered for the numerical simulations.

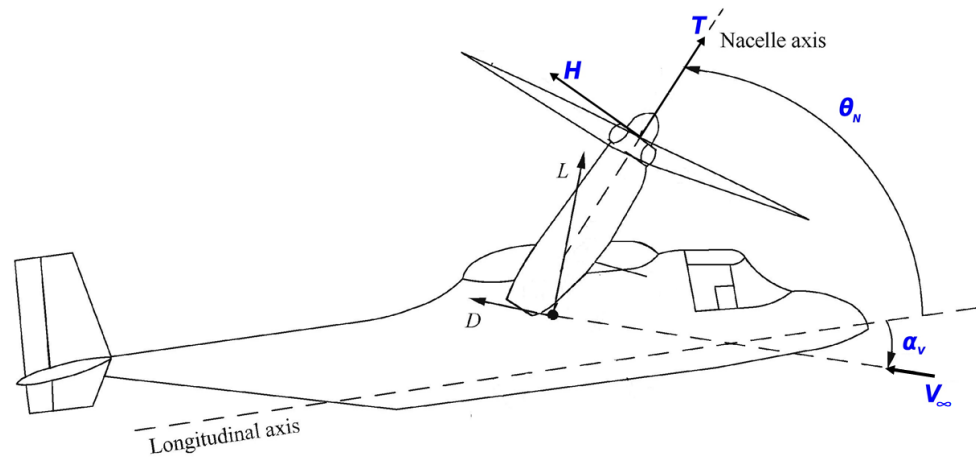| Flight Condition	V_∞	Vehicle Pitch Attitude (α_V)	Nacelle Angle (θ_N)	Rotor Speed Ω	Flap Angle	Flaperon Angle
Hover	0 knots	0°	90°	589 RPM	40°	25°
Conversion	40 knots	8.569°	75°	589 RPM	40°	25°
Conversion	100 knots	2.851°	60°	589 RPM	40°	25°
Conversion	140 knots	−0.773°	30°	589 RPM	40°	25°
Cruise	160 knots	4.332°	0°	517 RPM	0°	0°

Figure 5. Definition of the main parameters of the full XV-15 tiltrotor configuration.

The test conditions were considered from the Generic Tiltrotor (GTR) flight simulation data that were provided by Ferguson [46]. Following the same procedure that was suggested by the CFD works [16,17] for DUST simulations, the thrust (T) and H-force (H) on the wing-mounted proprotors were trimmed to the simulator data [46] by adjusting the rotor collective and longitudinal cyclic pitch angles. The lateral cyclic pitch angle was set to zero for all the simulated configurations, since the lateral cyclic control was not installed on the XV-15. The trim targets for the thrust and H-force of the single proprotor obtained by the DUST simulations are compared to the GTR data [46] in Figure 6 for all the flight conditions tested, as presented in the CFD work by Tran et al. [17]. Moreover, Figure 7 compares the average proprotor torque computed by DUST in these trimmed conditions to the GTR data [46] for all of the flight conditions considered and the flight test data available for the only cruise condition [48]. The quite good agreement of the torque behaviour provides confidence in the accuracy of the numerical models built for the DUST simulations.
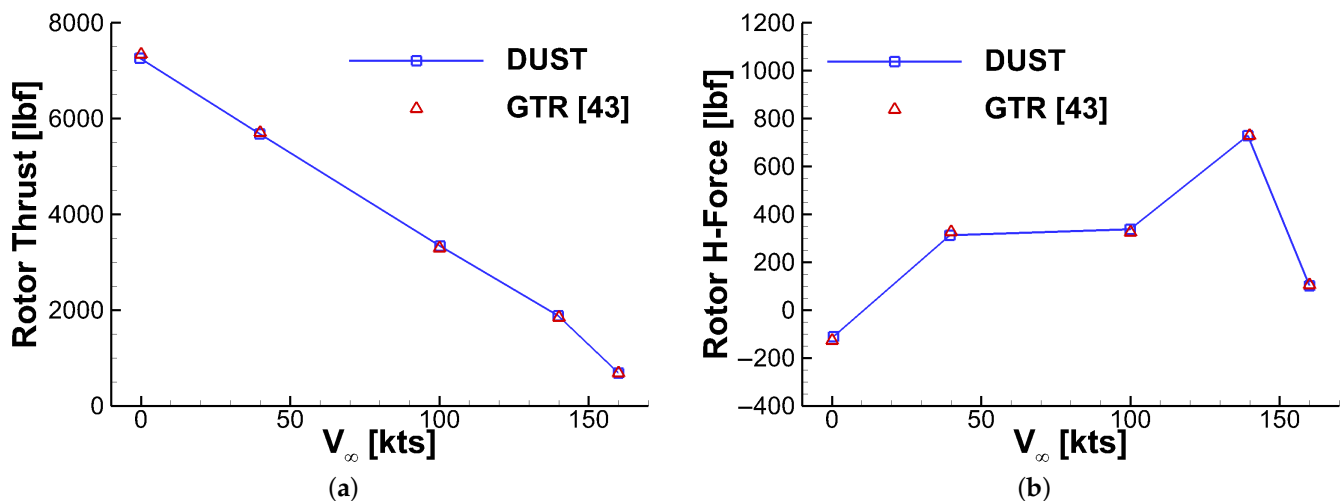

Figure 6. Trim targets for the proprotor thrust and H-force provided by Generic Tiltrotor (GTR) [46] compared with the results from the trimmed DUST simulations for all the flight conditions considered.
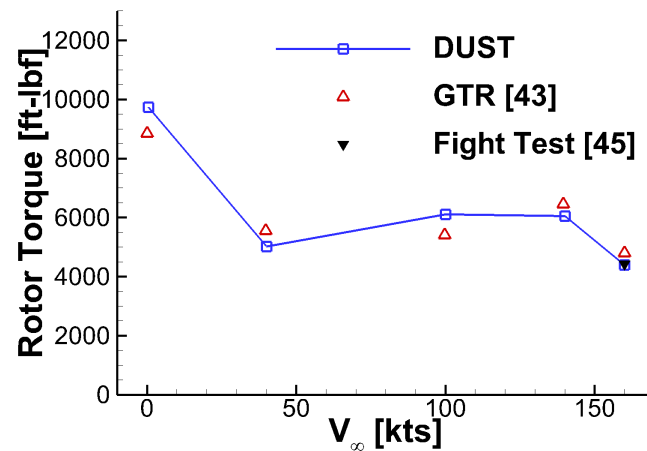
Figure 7. Comparison of the proprotor torque computed by DUST with GTR [46] and flight test data.

4. Results and Discussion

The present section shows the main results of the numerical simulations that were performed with DUST as compared to the CFD data. In the following figures, the palette of the colorbars used to present the DUST simulation results should not be exactly the same as that used for CFD, due to the fact that the CFD plots are pictures extracted from literature articles.

4.1. Wing-Proprotor Simulations

The results that are btained with DUST over the simplified configuration made by the wing and proprotor described in Section 4.1.1 are compared in the following to the outcomes of the work by Lim [18] to investigate the ability of the mid-fidelity approach to capture the principal mechanisms of rotor/wing aerodynamic interactions. In particular, the effects on the proprotor performance due to the wing could be separated from the effect provided by the proprotor on the wing airloads. Considering the effects of the wing on the proprotor performance, in airplane mode the presence of a thick airfoil, as used in the XV-15 tiltrotor configuration, produces a blockage effect that generates an effective upwash when the blade passes over the wing. This results in a positive peak in the normal force produced by the proprotor that occurs once per revolution on each blade. Moreover, due to the wing aerodynamic circulation, a doublet wash on the normal velocity of the blades—i.e. an upwash followed by a downwash—occurs when the blade passes in front of the wing, thus producing a local unsteady doublet of the blade normal force [18].

4.1.1. Wing Effect on Proprotor

Firstly, the effect of the wing on the global loads acting on the proprotor is investigated. Table 5 presents the comparison of the average thrust and power variations acting on the proprotor when the wing is installed, where the DUST values are evaluated by averaging the loads that are computed over the last two rotor revolutions.

Table 5. Comparison of the average proprotor global thrust and power variations due to the wing installation, $\alpha = 5°$, $V_\infty = 220$ kts, $\Omega = 517$ RPM.

	CFD		DUST	
	Δ	Δ %	Δ	Δ %
Thrust [lbs]	104	12.7	64.5	7.9
Power [hp]	64	8.1	41.7	5.4

The comparison of the average loads shows that DUST correctly captures the increase in both the proprotor thrust and torque due to the wing installation, coherent with the physics of the aerodynamic interaction. Only a slight underestimation of the load variation is observed with respect to CFD. This issue could be related to the relatively lower spatial discretisation used to model the blades and to the lower accuracy of the numerical model with respect to CFD. Moreover, Figure 8 shows the comparison of the variations in the rotor thrust and power calculated with the wing installed with respect to the single proprotor test case over the last rotor revolution. The behaviour of the time histories of the delta load curves that were provided by DUST clearly underlines the interference effect provided by the wing, as shown by the three peaks related to the passage of the three blades in front of the wing. These trends reproduce the results of CFD quite well, with small discrepancies concerning the amplitude of the delta values of both rotor thrust and power.
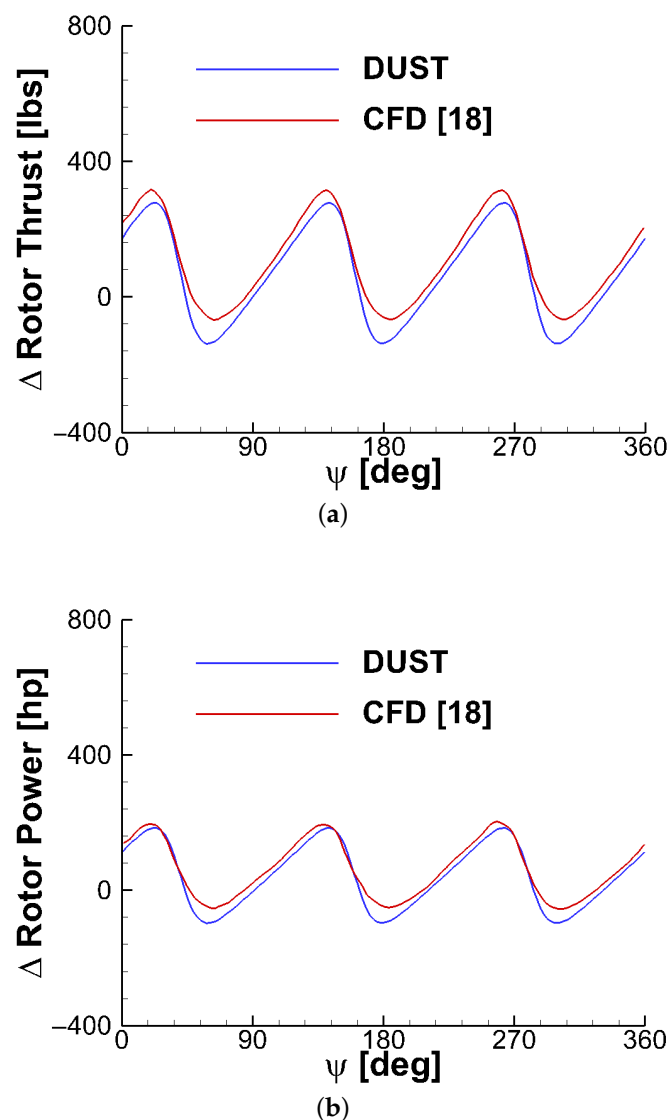

(a)

(b)

Figure 8. Comparison of the time history of the proprotor global thrust and power variations due to the wing installation, $\alpha = 5°$, $V_\infty = 220$ kts, $\Omega = 517$ RPM.

Figure 9a,b show a comparison of the contours of the blade non-dimensional normal force ($M^2 c_n$) computed over the last rotor revolution when the wing is installed in order to provide a detailed insight into the rotor/wing aerodynamic interaction effect on the local blade airloads. The DUST simulation results clearly show the doublet of the blade

normal force occurring in the region of azimuth around $\psi = 270°$ due to the passage of the blade in front of the wing. The global behaviour of the normal force contour plot is quite similar to the one computed by CFD, thus showing that lifting line modelling that is based on the use of tabulated aerodynamic sectional data considering viscosity effects is able to capture the variations in proprotor blade performance due to interactional flow phenomena. A more quantitative comparison is provided by Figure 9c,d, showing, respectively, the time histories of the blade $M^2 c_n$ computed for different radial stations in the outer region of the blade span and the radial distributions of the blade $M^2 c_n$ computed for different azimuthal angles of the blade along the last rotor revolution.

(**a**) $M^2 c_n$: CFD [18]

(**b**) $M^2 c_n$: DUST

(**c**)

(**d**)
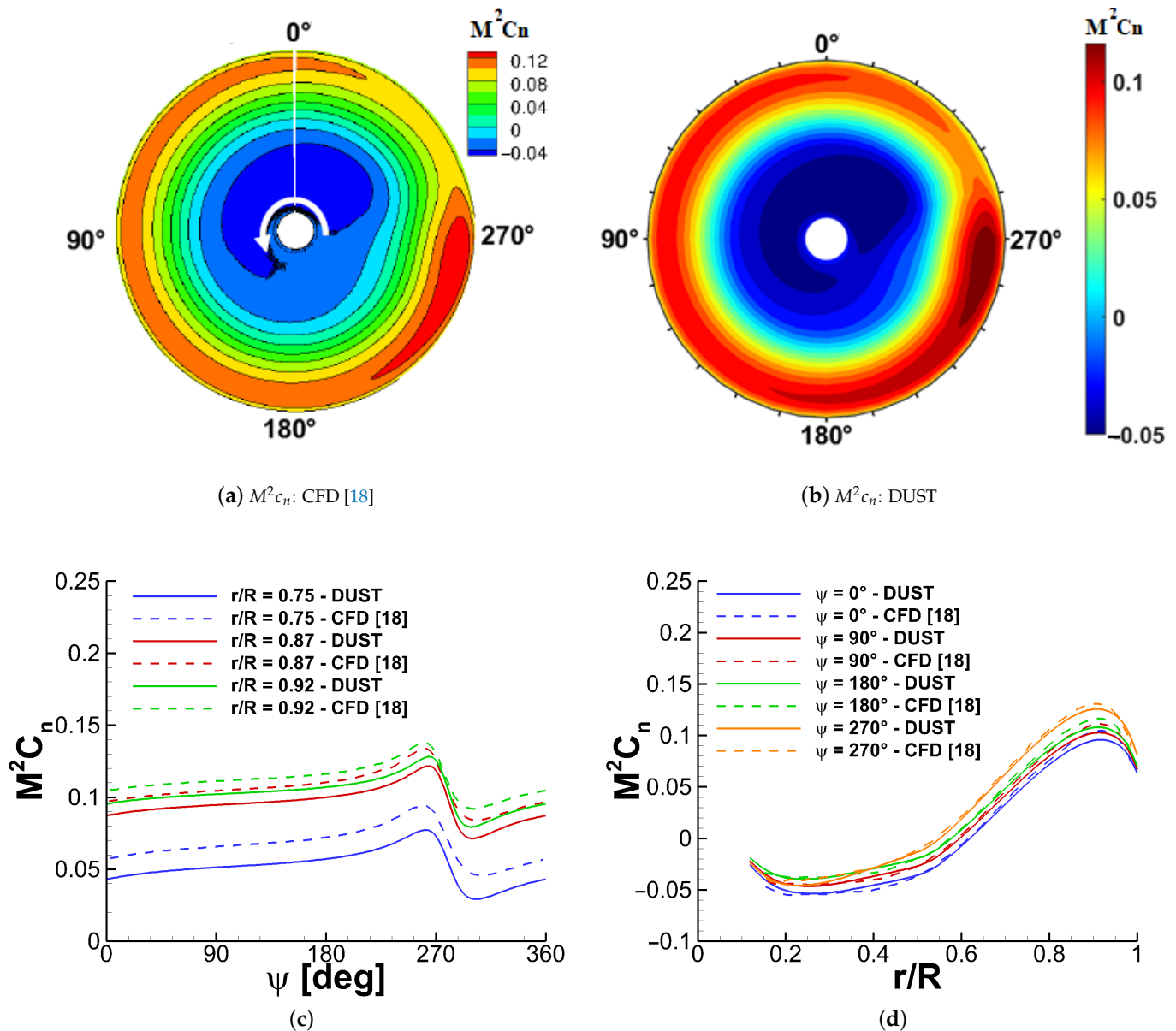
Figure 9. Comparison of the non-dimensional normal force $M^2 c_n$ on the proprotor blade, $\alpha = 5°$, $V_\infty = 220$ kts, $\Omega = 517$ RPM: (**a**) contour plot for CFD [18]; (**b**) contour plot for DUST; (**c**) time history; (**d**) radial distribution.

In particular, the comparison of the normal force time histories evaluated for all the three considered blade radial positions shows that DUST captures well both the amplitude and phase of the force doublet due to the blade passage computed by high-fidelity CFD. In particular, the time histories of the non-dimensional normal force of the proprotor computed by DUST show a downward shift in the curves with respect to CFD in the order

of 10% of the CFD values (see Figure 9c). This slight underestimation could be related to the spatial discretisation of the lifting line elements used to model the blades and to the lower accuracy of the numerical model with respect to CFD, as previously indicated concerning the global force acting on the proprotor. Moreover, the comparison of the radial distribution of the normal force that is provided in Figure 9d shows that DUST captures the increase in the normal load occurring at the outer region of the blade for $\psi = 270°$ well, corresponding to the passage of the blade in front of the wing. The behaviour of the normal force distributions along the different azimuthal angle considered in the comparison clearly shows quite good agreement between the DUST simulation and CFD results.

The comparison of the non-dimensional chord force ($M^2 c_c$) that is presented in Figure 10a for a single blade radial position—i.e., $r/R = 0.87$—shows a quite good agreement between the DUST and CFD results. Indeed, the amplitude and phase of the chord force doublet due to the wing installation are captured quite well by DUST. The non-dimensional pitching moment comparison ($M^2 c_m$) that is presented in Figure 10b shows a slight underestimation of the doublet amplitude and a downward shift in the curve computed by DUST with respect to CFD results. The mismatch observed for the pitching moment is related to the combined effects of the discrepancies that are related to the normal and chordwise components of the aerodynamic force acting on the blades.
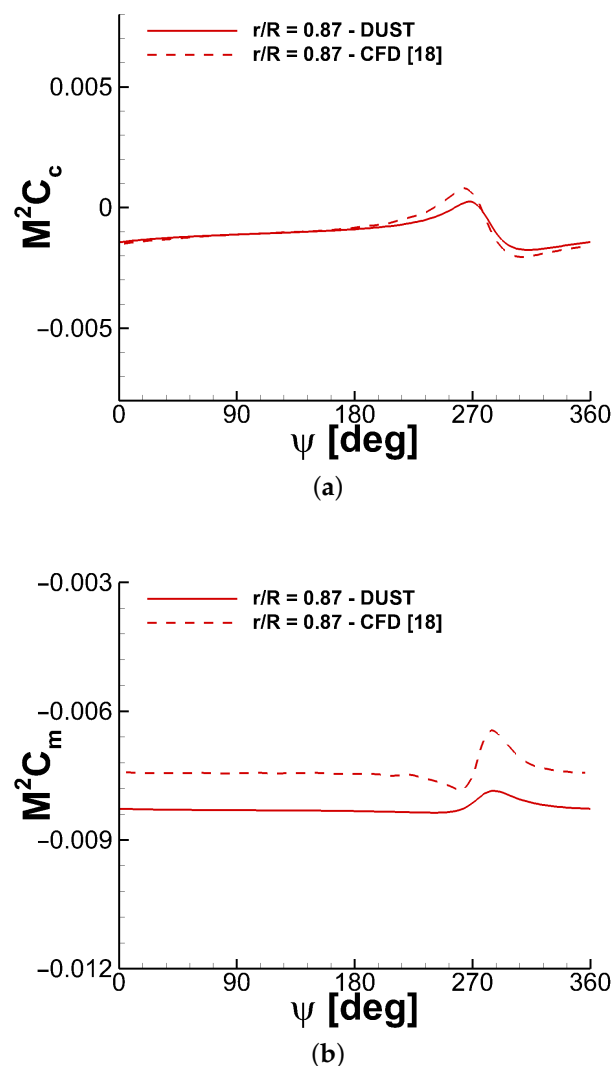

(a)

(b)

Figure 10. Comparison of the time histories of the non-dimensional chord force $M^2 c_c$ and pitching moment $M^2 c_m$ on the proprotor blade at $r/R = 0.87$, $\alpha = 5°$, $V_\infty = 220$ kts, $\Omega = 517$ *RPM*.

4.1.2. Proprotor Effect on Wing

The effect of the proprotor on the normal force acting on the wing is investigated in the following. The DUST simulations showed a decrease in the average lift acting on the wing of 2.5% due to the proprotor installation, while a slightly positive increase of 0.7% was calculated by CFD [18]. Thus, in order to obtain more detailed insight into the capabilities of a mid-fidelity approach to capture the flow physics related to the aerodynamic interaction effect of the proprotor on the wing, Figure 11a shows a representation of the flow field that is computed by DUST at $\psi = 310°$ by means of the iso-surface of the Q-criterion and the contours of the slipstream perturbation velocity on a horizontal $X - Y$ plane over the wing. This flow field representation clearly shows the interference of the proprotor helical system on the wing that mainly provides an upwash due to the blade tip vortex encountering the inboard region of the wing. This feature provides an increase in the slipstream velocities over the wing with respect to freestream in the inboard region of the wing between $2Y/b = 0.2$ and $2Y/b = 0.4$. This augmented velocity in the streamwise direction provides a local increase in the dynamic pressure and, consequently, an increase in the wing lift at the inboard region. The comparison of the span-wise sectional normal force distribution computed at $\psi = 310°$ shown in Figure 11b reflects this flow physics effect. Indeed, an increase in the wing loading at the inboard region is observed when the proprotor is installed. This effect is captured by DUST simulations, even if the positive peak loading at inboard region is slightly lower with respect to CFD. Moreover, the interaction of the vortices that are issued by the proprotor blade root, as clearly observed from the Q-criterion iso-surface shown in Figure 11a, provides a decrease in the normal force with respect to the single wing configuration at the outboard region of the wing. This effect is well captured by the DUST simulations, as shown by the quite good agreement of the normal force distribution with the CFD results in the range between $2Y/b = 0.6$ and $2Y/b = 1$. Therefore, the comparison of the span-wise behaviour of the normal force acting on the wing that is shown in Figure 11b indicates that the mid-fidelity approach implemented in DUST is able to capture the physical effects of the aerodynamic interaction of the proprotor on the wing, while the slight decrease in the global normal force acting on the wing calculated by DUST is mainly due to the slight underestimation of the peak loading occurring at the inboard region. The reduced peak loading that is computed by DUST could be related to the spatial discretisation of the surface panels used to model the wing. Nevertheless, a further investigation of the possible dependence of the solution from the meshing properties of the numerical model is out of the main scope of the work, consisting of the assessment of a light numerical solver aimed at the investigation of the interactional flow physics that are involved in the tiltrotor aerodynamics used for the preliminary design of novel vehicles.

Figure 12 provides a confirmation of DUST's ability to capture the flow physics related to this aerodynamic interaction , showing a comparison of the sectional normal force contours acting on the semi-span wing calculated for the last proprotor revolution. The impulsive positive peak loading provided by the blade tip vortex impact is clearly captured by the DUST simulations, showing a 3-per-rev footprint that is characterised by the same intensity and position at the inboard span-wise region of the wing ($0.2 < 2Y/b < 0.4$) highlighted by the CFD results. Moreover, the representation of the DUST results also captures the extent and intensity of the loading decrease occurring toward the wing-outboard due to the effect of the interaction of the vortices that are issued at the blade root.
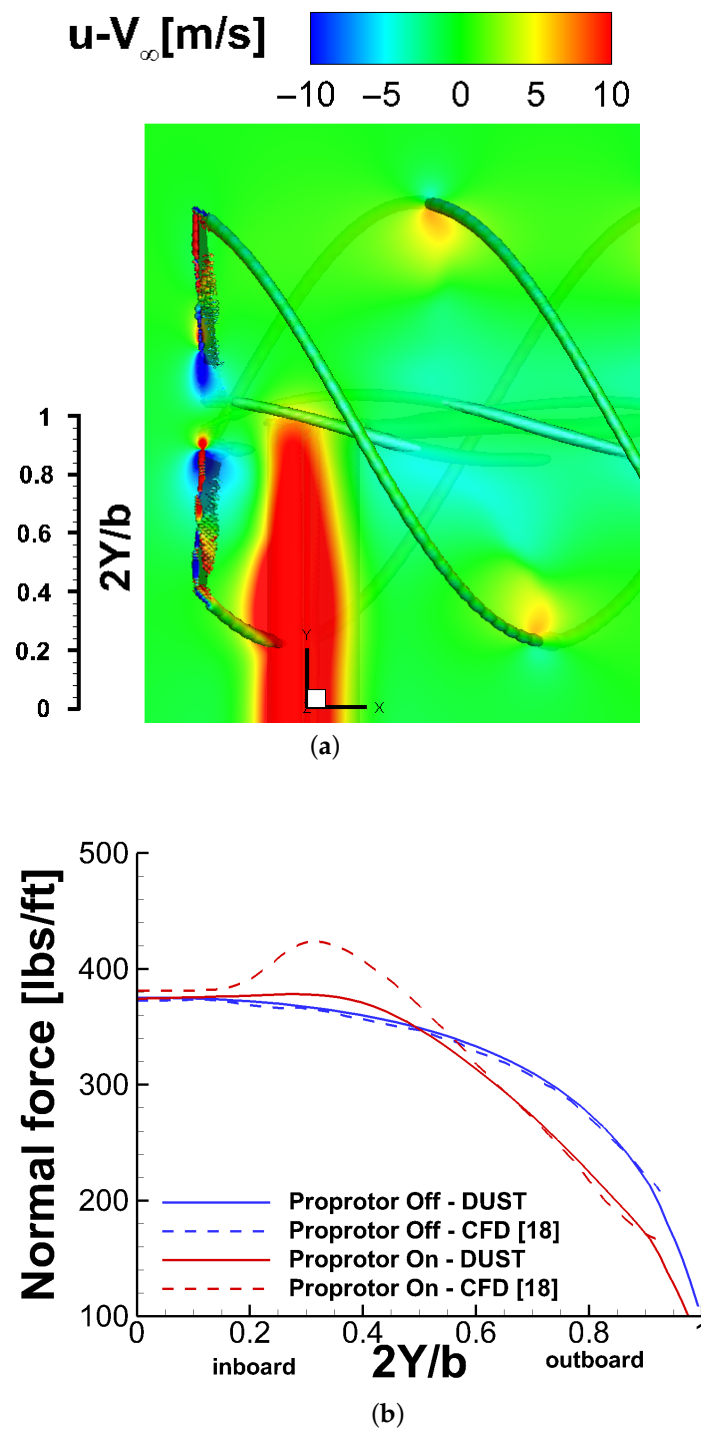
(a)

(b)

Figure 11. Numerical results for blade azimuth $\psi = 310°$, $\alpha = 5°$, V_∞ = 220 kts, Ω = 517 RPM: (**a**) iso-surface of Q-criterion with contours of the slipstream perturbation velocity over an $X - Y$ plane at 0.6 m from the proprotor center computed by DUST; (**b**) comparison of the spanwise normal force distribution on the wing.
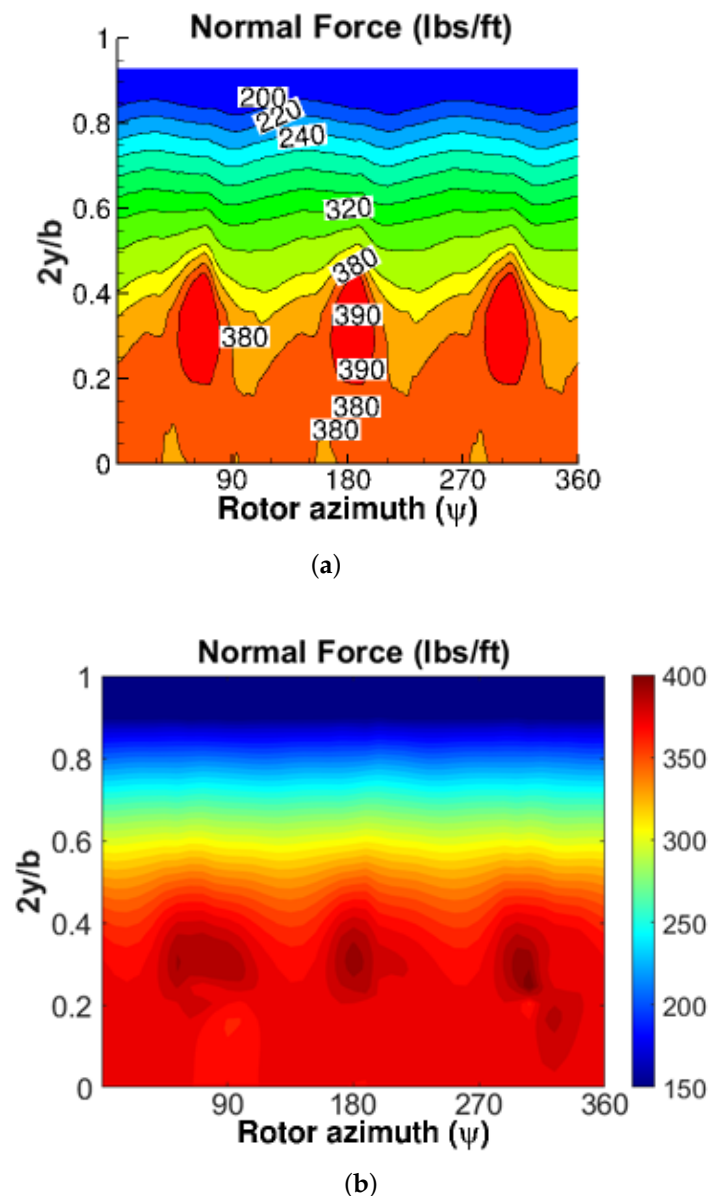
(a)

(b)

Figure 12. Comparison of the contours of the sectional normal force on the wing during the last proprotor revolution, $\alpha = 5°$, V_∞ = 220 kts, Ω = 517 RPM. (**a**) CFD [18]; (**b**) DUST.

4.2. Full Vehicle Simulations

The results obtained with DUST over the XV-15 full vehicle for the different flight conditions reported in Table 4 are compared in the following to the CFD simulation results. In particular, for hover and cruise flight conditions, the comparison is performed with the outcomes of the work by Tran et al. [17], while, for conversion flight conditions, the more recent work proposed by Tran and Lim [16] is used as a reference for comparison, as it is considered to be more accurate.

4.2.1. Hover Condition

In hover flight conditions, strong aerodynamic interactions between the proprotors and wing characterise the flow field around the airframe. Figure 13 shows the comparison of the contours of the instantaneous vertical velocity component around the vehicle computed in hover for the blade azimuth $\psi = 270°$ over a $Y - Z$ plane passing through the nacelle axis.
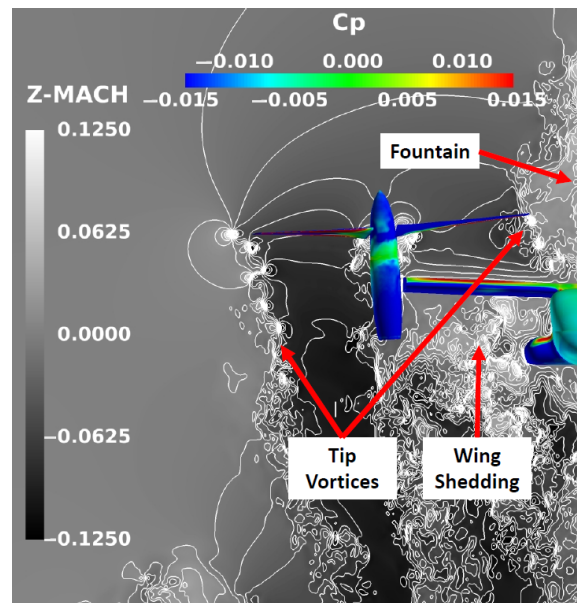
(**a**)
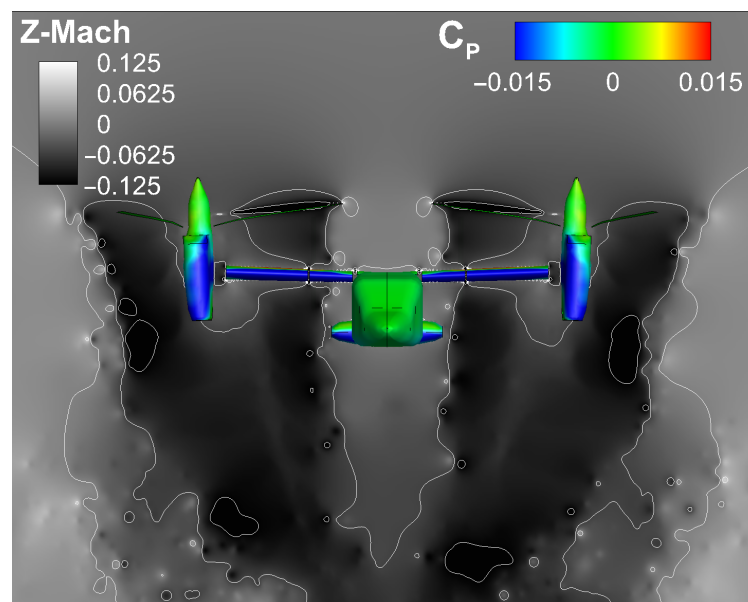
(**b**)

Figure 13. Comparison of the contours of the vertical velocity component around the vehicle in hover at $\psi = 270°$, $\theta_N = 90°$, $\Omega = 589$ RPM. (**a**) Half-span model: CFD [17]; (**b**) Complete model: DUST.

The DUST representation closely resembles the global behaviour of the flow field around the vehicle that is computed by CFD. In particular, the DUST results obtained over the complete vehicle model show a flow region over the fuselage characterised by a quite moderate upwash. This flow feature typical of tiltrotor configurations is known as fountain flow [6]. The size and strength of the fountain flow is greater in half-span CFD models due to the reflection of the flow caused by the symmetry boundary condition [6]. The hover flight condition is characterised by a not symmetrical behaviour of the flow field as shown both by CFD simulations of Potsdam and Strawn [6] and by flow visualizations of Polak et al. [49]. Indeed, a significant higher upwards velocity region over the fuselage is observed from the half-span CFD solution shown in Figure 13a. Therefore, the lower computational effort required by a mid-fidelity approach enabled us to obtain a better representation of this characteristic flow feature with respect to the CFD simulations over

half-span models. The ability to obtain a quite good representation of the overall flow field around the complete vehicle has to be considered a point of strength of the use of a mid-fidelity approach to aerodynamics for the preliminary design of a tiltrotor aircraft.

Considering now the vehicle aerodynamic performance, the interference of the wing on the rotor downwash provides a significant download on the vehicle that must be overcome by the rotor in the hover and climb phases of the tiltrotor flight missions. Figure 14 shows the comparison of the instantaneous surface pressure on the fuselage computed by DUST and CFD in hover for the blade azimuth $\psi = 270°$. A large high-pressure region covering almost all of the wing surface can be observed due to the impingement of the rotor wake. The high-pressure region extent and the positive C_p values over the wing are quite high for CFD with respect to the DUST results. Consequently, the download on the wing computed by DUST is lower with respect to CFD. Indeed, the download on the wing computed by DUST resulted in being about 3% of the global proprotor thrust, while CFD provided a download of 10.3%. This difference could be related to an incorrect prediction of the aerodynamic effects that are related to the wing surface that, in this flight condition, is normally invested by the proprotor wake. As a matter of fact, for this flight condition, the complex flow field around the wing is characterised by low velocities and low Reynolds numbers and, particularly, by a massive wing shedding region (see Figure 13a) and flow separations. Consequently, as could be expected, these flow conditions typical of hover have to be considered difficult to represent with potential methods. Moreover, CFD shows a higher-pressure region over the fuselage upper surface (see Figure 14a) due to the higher strength of the fountain flow effect that is related to the use of a half-span CFD model. This feature could negatively affect the evaluation of the global download of the vehicle that was obtained by CFD with respect to the real aircraft.
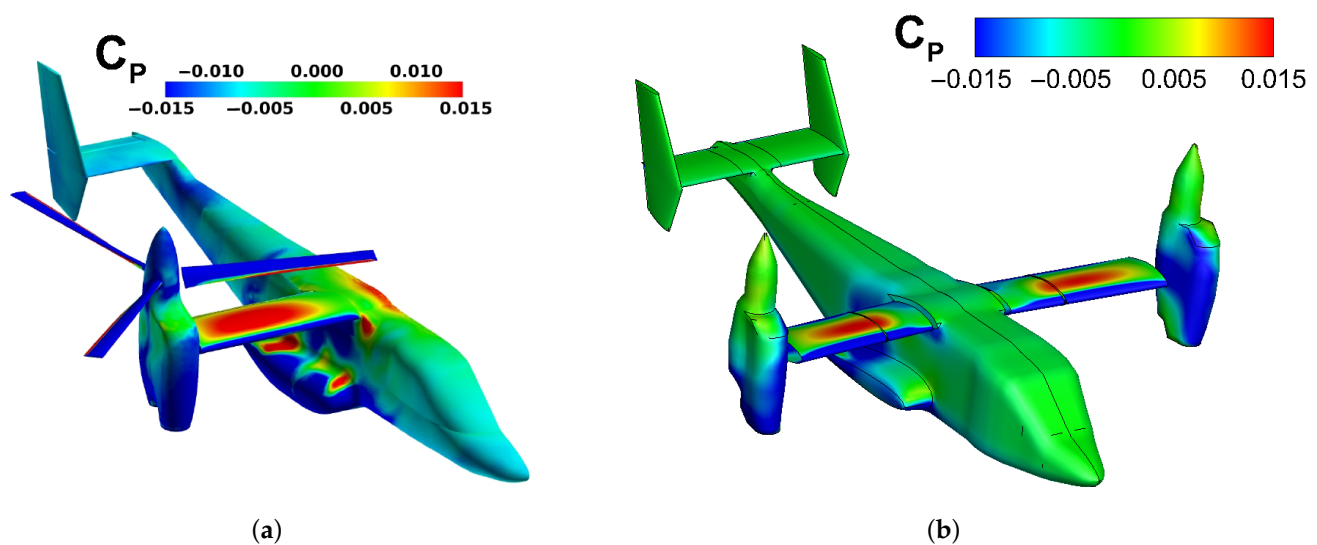

(a)   (b)

Figure 14. Comparison of the contours of the pressure coefficient C_p on the vehicle surface in hover at $\psi = 270°$, $\theta_N = 90°$, $\Omega = 589$ RPM. (**a**) Half-span model: CFD [17]; (**b**) Complete model: DUST.

Figure 15 shows a comparison of the contours of the blade non-dimensional normal force ($M^2 c_n$) and pitching moment ($M^2 c_m$) computed over the last rotor revolution in order to provide detailed insight into the evaluation of the proprotor aerodynamic performance in hover. The general behaviour of the polar distributions of the normal force and pitching moment computed by CFD is captured by the DUST simulation. Nevertheless, the CFD results show a sudden fluctuation in both the normal force and pitching moment, particularly apparent in the azimuthal region around $\psi = 270°$. These fluctuations are related to the combination of the blade passage over the high-pressure region on the wing and the reingestion of the fountain flow, as indicated by Tran et al. [17]. The amplitude and dynamics of the impulsive loading of the blades could be overestimated by CFD due to

the greater size and strength of the fountain flow related to the half-span model, as indicated in [6]. On the other hand, since the fountain size and dynamics are weaker for the full-span vehicle, the DUST simulation results do not show these fluctuations in this azimuthal region, and the global behaviour of the normal force and pitching moment are smoother with respect to the CFD results. Consequently, the differences observed in the polar representation of the blade force distributions could be mainly related to the use of a half-span model for CFD simulation with respect to the full aircraft configuration that is used for the DUST calculations.
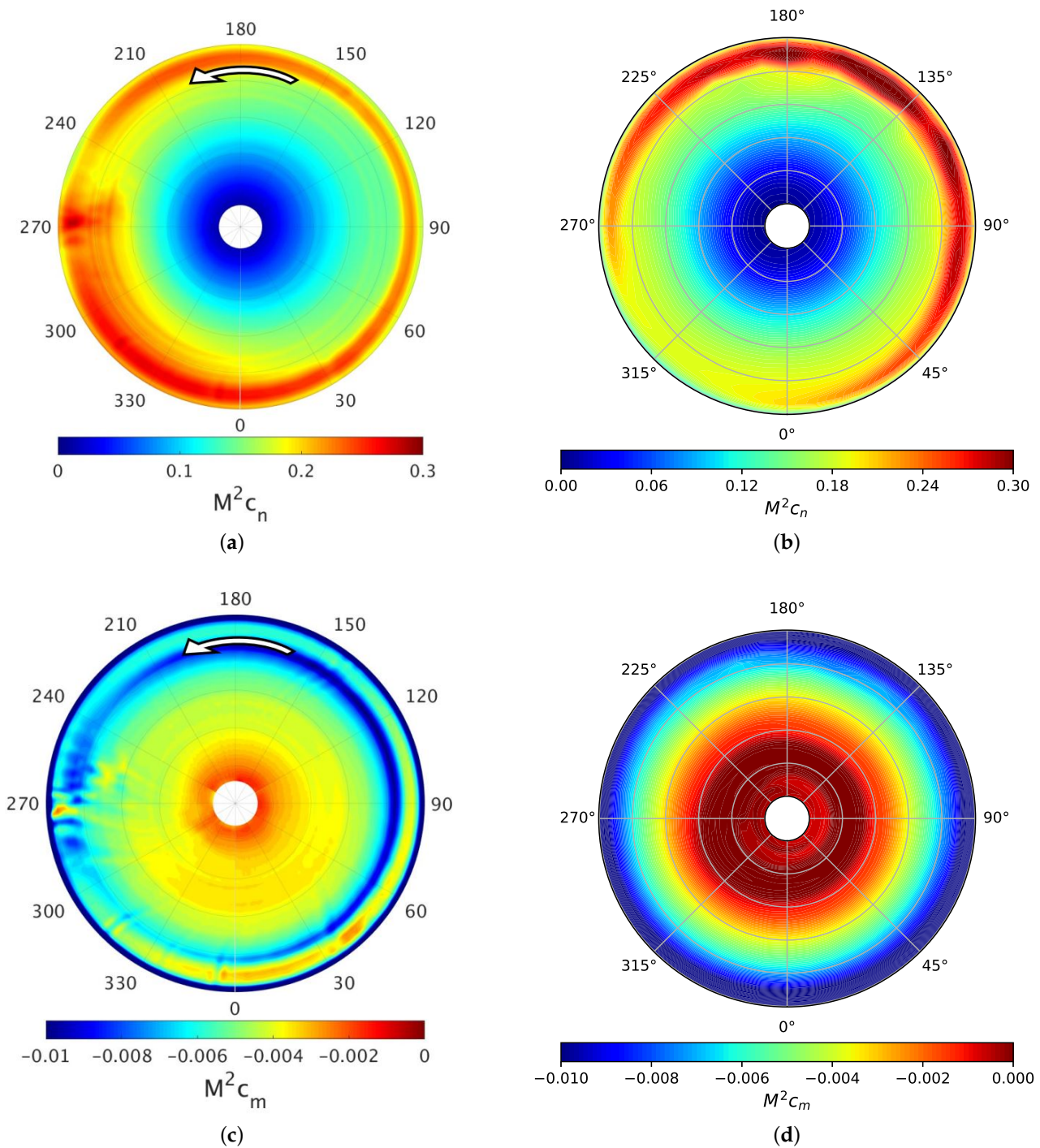

Figure 15. Comparison of the contours of the non-dimensional normal force $M^2 c_n$ and pitching moment $M^2 c_m$ on the proprotor blade in hover, $\theta_N = 90°$, Ω = 589 RPM. (**a**) $M^2 c_n$: CFD [17]; (**b**) $M^2 c_n$: DUST; (**c**) $M^2 c_m$: CFD [17]; (**d**) $M^2 c_m$: DUST.

4.2.2. Conversion Mode Conditions

Three flight configurations were considered by the DUST simulations throughout the conversion phase of the tiltrotor aircraft, as reported in Table 4. The results of the DUST simulations obtained over the three aircraft flight configurations characterised by a different nacelle angle and freestream velocity are thoroughly compared in the following with the CFD results from the recent work by Tran and Lim [16]. In particular, differently from hover and cruise conditions, the comparison of the polar representation of the loads acting on the blade in conversion mode are not presented, since they are not available from the work by Tran and Lim [16].

Nacelle angle $\theta_N = 75°$, freestream velocity V_∞ = 40 kts.

The combination of the high incidence angle of the nacelle with the low freestream velocity provides complex vortex interactions. Indeed, the vortices that are issued by the proprotor blades quickly wrap up into a pair of "disk vortices" starting particularly close to $\psi = 90°$ and $\psi = 270°$.

This feature, which was well described in the CFD activities that were reported in [16,17], was clearly captured by the DUST simulation results, as can be observed from the instantaneous flow field computed at $\psi = 270°$ represented by the iso-surface of the Q-Criterion in Figure 16. In particular, at $\psi = 90°$ and $\psi = 270°$, a proprotor blade interacts significantly with the vortices that were issued by the second and third blade of the proprotor passing simultaneously on both the upper and lower surface of the rotor blade. The flow physics of this interaction is quantitatively captured by the DUST simulation, as shown by the contours of vorticity illustrated in Figure 16b at the azimuthal angle $\psi = 270°$. The coherent representation of the flow field computed by DUST confirms the suitability of the implemented physics-based model for proprotor wakes to correctly simulate the complex interactions that characterise the conversion flight conditions with a computational cost that is greatly lower with respect to CFD. The interactions that are related to the formation of disk vortices create large variations in the normal force acting on the proprotor blade. This effect is clearly visible from the comparison of the blade $M^2 c_n$ computed at $r/R = 0.95$, as shown in Figure 17a. The DUST simulations capture well the occurrence and amplitude of the normal force variations around $\psi = 90°$ and $\psi = 270°$ computed by CFD. Moreover, the amplitude of the sudden fluctuations in the pitching moment are not well captured by DUST, even if the mean value along the rotor revolution is quite similar to the CFD results. The incorrect representation of the pitching moment peak loading could also be affected by the prediction of a chord-wise force component that is not available for comparison from CFD.
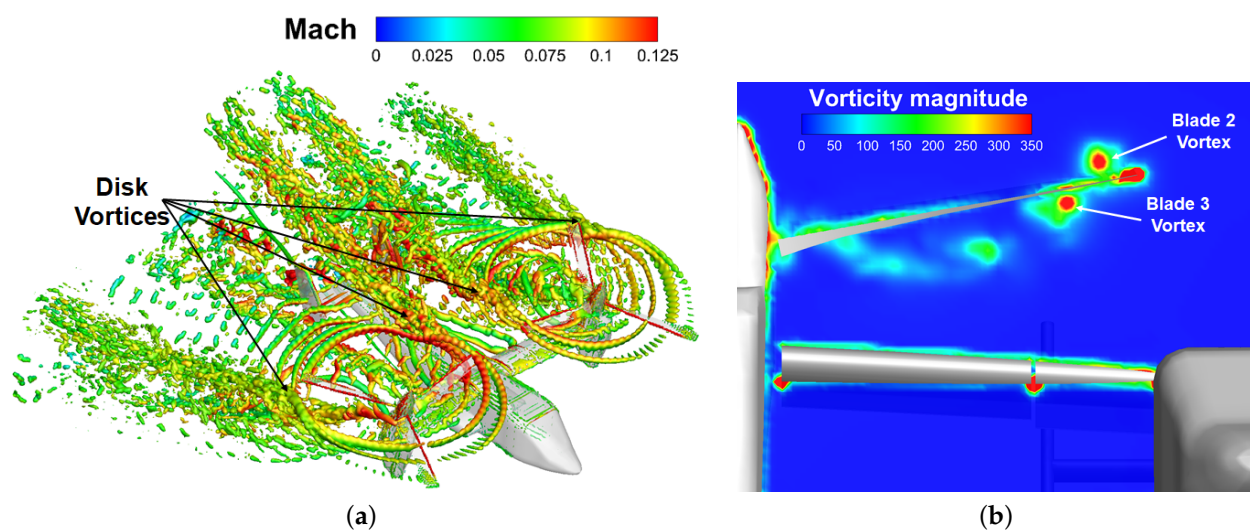

(**a**)　　　　　　　　　　　　　　(**b**)

Figure 16. Instantaneous flow field computed by DUST in conversion flight condition at $\psi = 270°$, $\theta_N = 75°$, V_∞ = 40 kts, Ω = 589 RPM: (**a**) iso-surface of Q-Criterion, (**b**) iso-contours of vorticity on a slice cutting the nacelle axes.
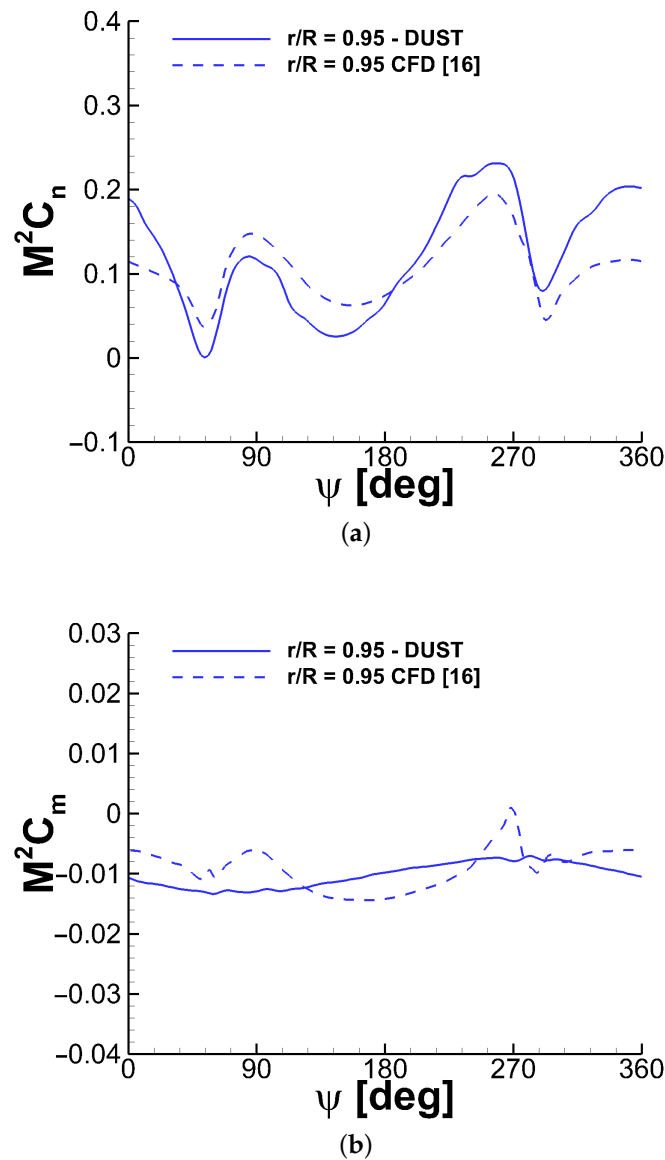
(a)

(b)

Figure 17. Comparison of the time histories of the non-dimensional normal force $M^2 c_n$ and pitching moment $M^2 c_m$ on the proprotor blade in conversion flight condition at $r/R = 0.95$, $\theta_N = 75°$, $V_\infty = 40$ kts, $\Omega = 589$ RPM.

In order to evaluate the aerodynamic effect between the proprotor wake and wing, Figure 18 shows the comparison of the instantaneous flow field on a slice cutting the wing longitudinally at midspan. A quite good agreement is observed between the CFD and DUST flow field representations, showing, for this flight condition, that the proprotor wake is advected downstream, completely missing the wing. Nevertheless, the DUST results do not show the limited separated flow region over the upper surface of the deflected flap, as can be expectable from potential methods.
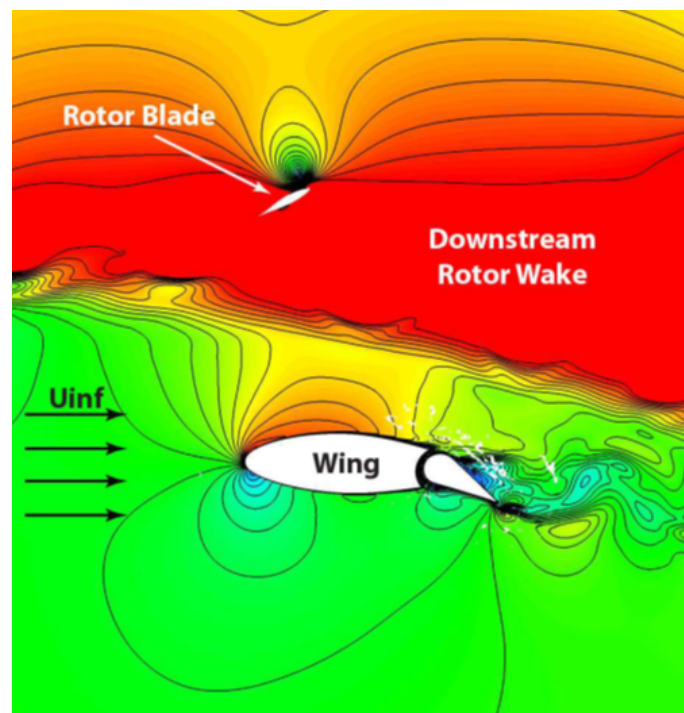
(a)
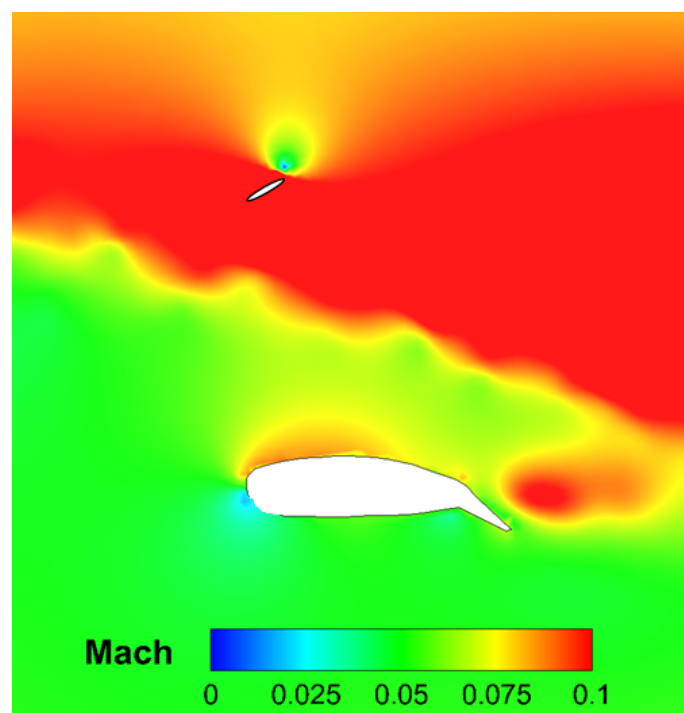
(b)

Figure 18. Comparison of the instantaneous flow field at wing midspan in conversion flight conditions at $\psi = 270°$, $\theta_N = 75°$, $V_\infty = 40$ kts, $\Omega = 589$ RPM. (**a**) CFD-[16]; (**b**) DUST.

Nacelle angle $\theta_N = 60°$, freestream velocity V_∞ = 100 kts.
 The decrease in the nacelle angle combined with the increase in the free-stream velocity allows for the distance between the tip vortices to increase with respect to the previous flight condition, thus preventing the interactions between the vortices and the formation of disk vortices. This flow behaviour, in good agreement with the CFD results [16], is clearly

visible in Figure 19, showing a representation of the instantaneous flow field at $\psi = 270°$ by means of the iso-surface of Q-Criterion.
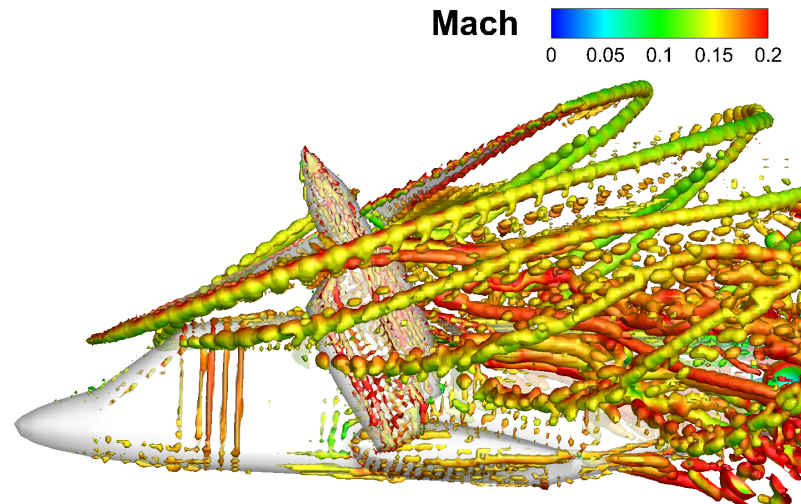

Figure 19. Instantaneous flow field that is computed by DUST in conversion flight condition at $\psi = 270°$, $\theta_N = 60°$, $V_\infty = 100$ kts, $\Omega = 589$ RPM; iso-surface of Q-Criterion.

The three-dimensional flow representation also shows the massive shedding that occurs behind the wing control surfaces and the nacelle. Furthermore, in this flight condition, the lower angle of the nacelle causes the blades to pass in front of the wing. Consequently, the rotor downwash invests the wing and accelerates the flow over the upper surface.

This flow behaviour around the wing is well captured by the DUST simulations, as shown in Figure 20 by the instantaneous flow field that is illustrated on a slice cutting the wing longitudinally at midspan. Nevertheless, also for this case, the DUST results do not show the limited separated flow region that is outlined by the CFD results over the upper surface of the deflected flap.
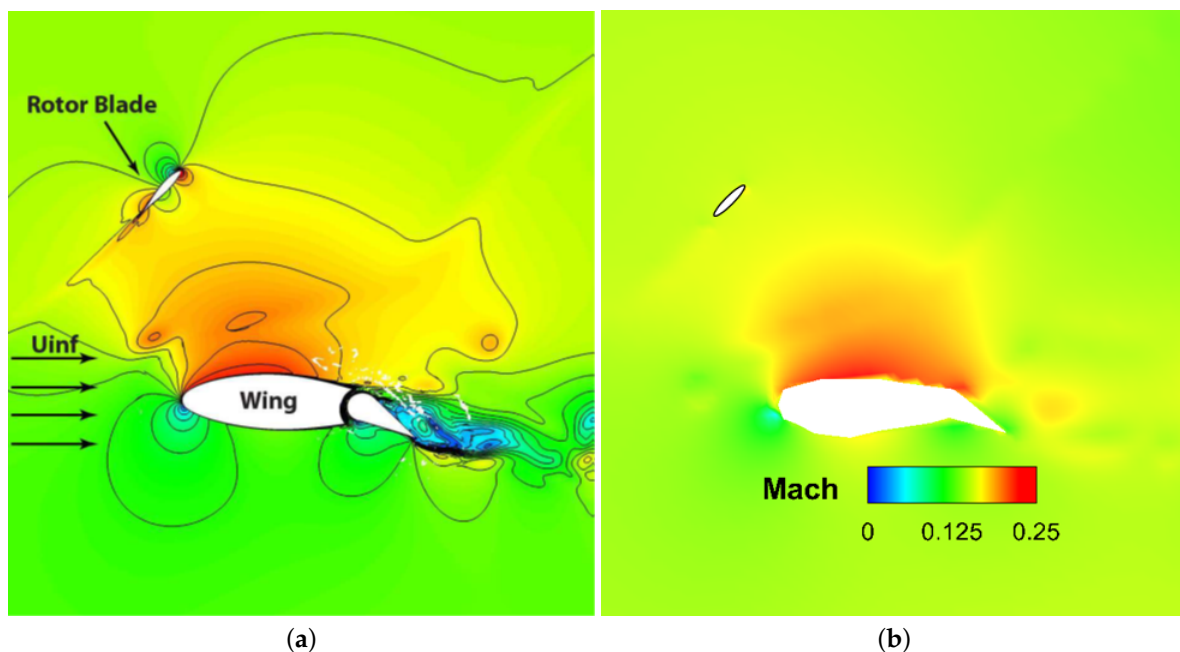

Figure 20. Comparison of the instantaneous flow field at wing midspan in conversion flight condition at $\psi = 270°$, $\theta_N = 60°$, $V_\infty = 100$ kts, $\Omega = 589$ RPM. (**a**) CFD-[16]; (**b**) DUS.

The comparison of the non-dimensional blade normal force $M^2 c_n$ and pitching moment $M^2 c_m$ at $r/R = 0.95$ in Figure 21 shows a quite good agreement between the DUST and CFD results. Indeed, the DUST simulations capture the large oscillations of both the blade normal load and pitching moment throughout the proprotor blade revolution well. Nevertheless, concerning pitching moment representation, a smaller amplitude and a small phase shift in the curve behaviour is observed. These small differences could be explained analogously to the results discussion of the previous configuration while also taking the lower accuracy of the numerical model with respect to CFD into account.
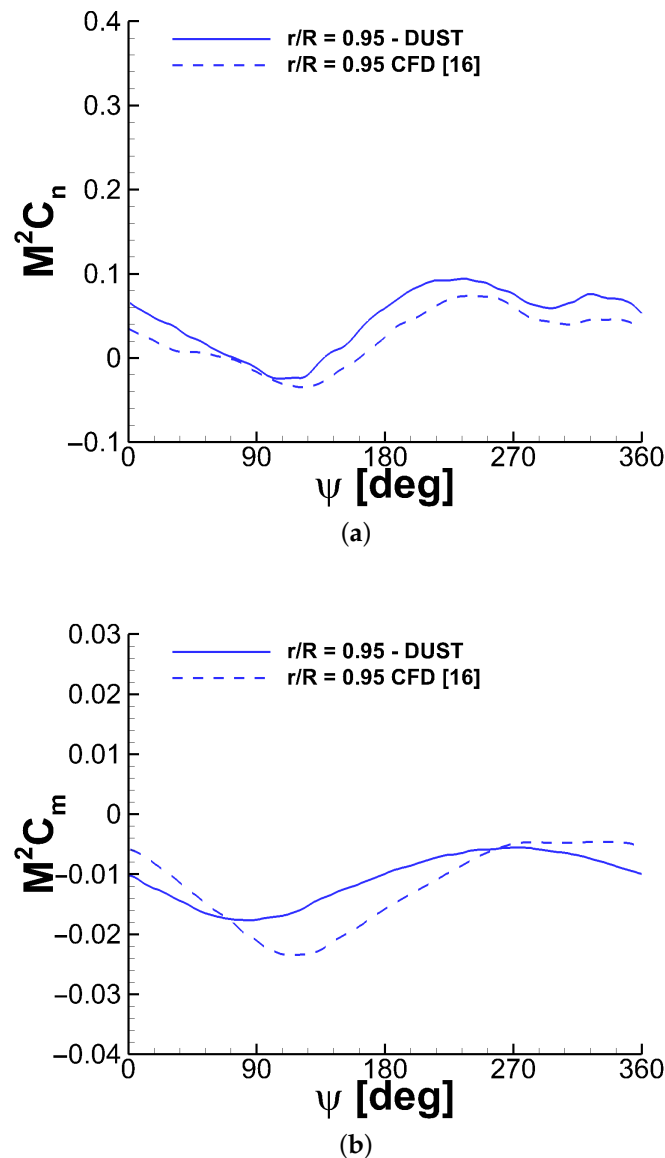

(a)

(b)

Figure 21. Comparison of the time histories of the non-dimensional normal force $M^2 c_n$ and pitching moment $M^2 c_m$ on the proprotor blade in conversion flight condition at $r/R = 0.95$, $\theta_N = 60°$, V_∞ = 100 kts, Ω = 589 RPM.

Nacelle angle $\theta_N = 30°$, freestream velocity V_∞ = 140 kts.
In this flight condition, the low nacelle angle and high freestream velocity prevent interactions between the tip vortices that show a quite coherent helical path.

This flow behaviour can be observed from the instantaneous velocity field that is computed by DUST at $\psi = 270°$, as shown in Figure 22. The flow field representation

shows that a massive shedding behind the wing control surfaces and nacelle is still present, even if it decreased with respect to the analysed flight conditions in the first stages of the conversion phase.
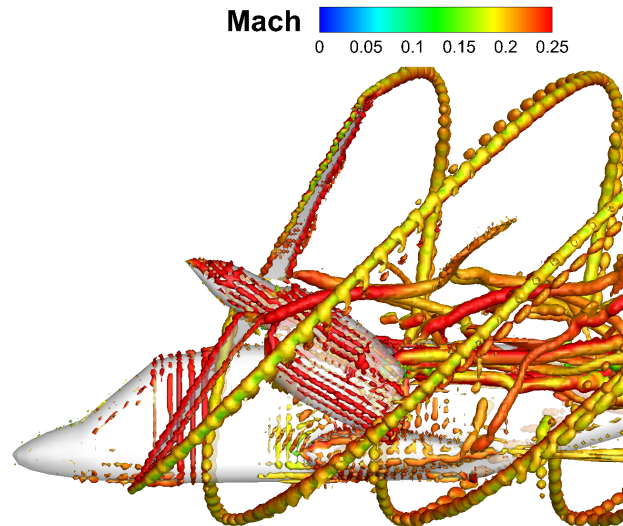

Figure 22. Instantaneous flow field computed by DUST in conversion flight condition at $\psi = 270°$, $\theta_N = 30°$, V_∞ = 140 kts, Ω = 589 RPM; iso-surface of Q-Criterion.

The large oscillations and behaviour of both the blade normal load and pitching moment occurring throughout the proprotor blade revolution are well captured by DUST simulations, as can be observed from the comparison that is presented in Figure 23. In particular, in this flight condition both DUST and CFD show a doublet loading at $\psi = 270°$ for the $M^2 c_n$ due to the interactional aerodynamic effect of the wing. Additionally, for this flight configuration, the pitching moment representation of DUST simulation shows a smaller amplitude and a small phase shift in the curve behaviour.

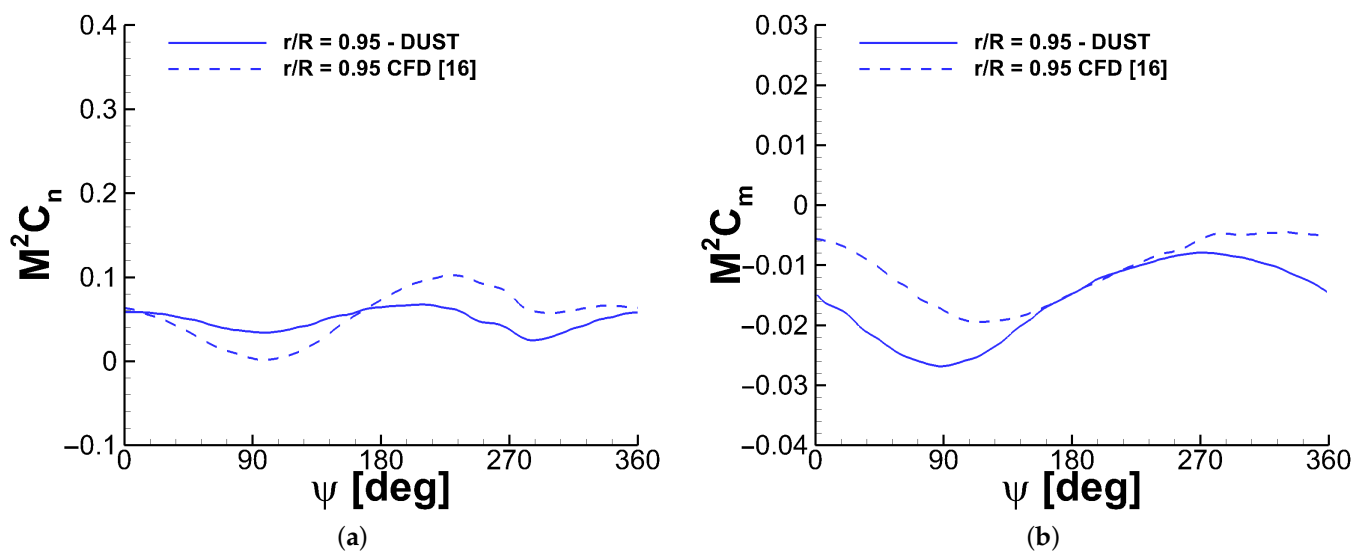**Figure 23.** Comparison of the time histories of the non-dimensional normal force $M^2 c_n$ and pitching moment $M^2 c_m$ on the proprotor blade in conversion flight condition at $r/R = 0.95$, $\theta_N = 30°$, V_∞ = 140 kts, Ω = 589 RPM.

4.2.3. Cruise Condition

In the cruise condition, the proprotor wake is advected downstream and it shows the coherent helical structure of the vortices that are issued by the blade tips that invest the wing.

This flow behaviour is clearly reproduced by the DUST simulations, as shown by the iso-surface of the Q-criterion that is illustrated in Figure 24 for $\psi = 270°$. Moreover, the wing control surfaces are not deflected and the nacelle axis is aligned with the freestream velocity, thus only the shedding from the nacelle is still visible and it significantly decreased with respect to the analysed conversion mode flight conditions.
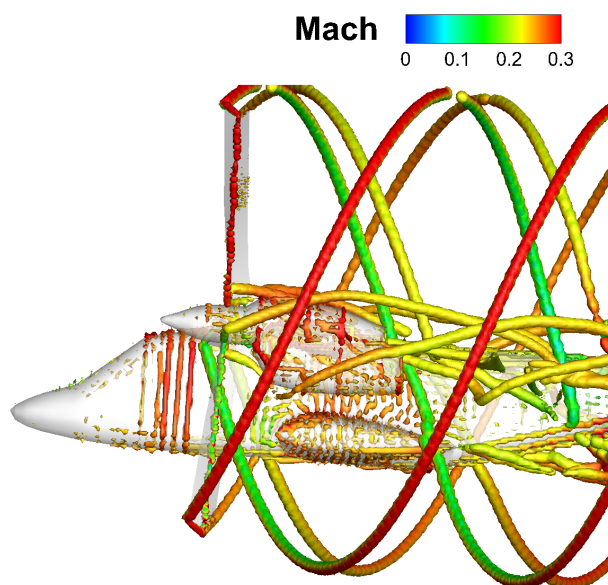

Figure 24. Instantaneous flow field computed by DUST in cruise flight condition at $\psi = 270°$, $\theta_N = 0°$, $V_\infty = 160$ kts, $\Omega = 517$ RPM; iso-surface of Q-Criterion.

The aerodynamic interaction between proprotor and wing creates an effect on the blade performance similar to what was described for the simpler proprotor/wing configuration in Section 4.1.1. Indeed, the comparison of the contours of the blade non-dimensional normal force and pitching moment computed over the last rotor revolution shows a doublet loading, particularly for $M^2 c_n$ (see Figure 25), which was related to the passage of the blade in front of the wing. This feature and the general behaviour of the load polar distributions computed by DUST and CFD are in quite good agreement, with some limited discrepancies being observed for the pitching moment only that, similarly to what was observed in Section 4.1.1, could be related to a combined effect of a slight disagreement of both normal and chord-wise force components. Nevertheless, the outcomes of this comparison confirm the capabilities of the mid-fidelity approach that was implemented in DUST to reproduce the flow features related to proprotor/wing interactions and also capture the behaviour of the rotor aerodynamic performance for full-vehicle cruise conditions.
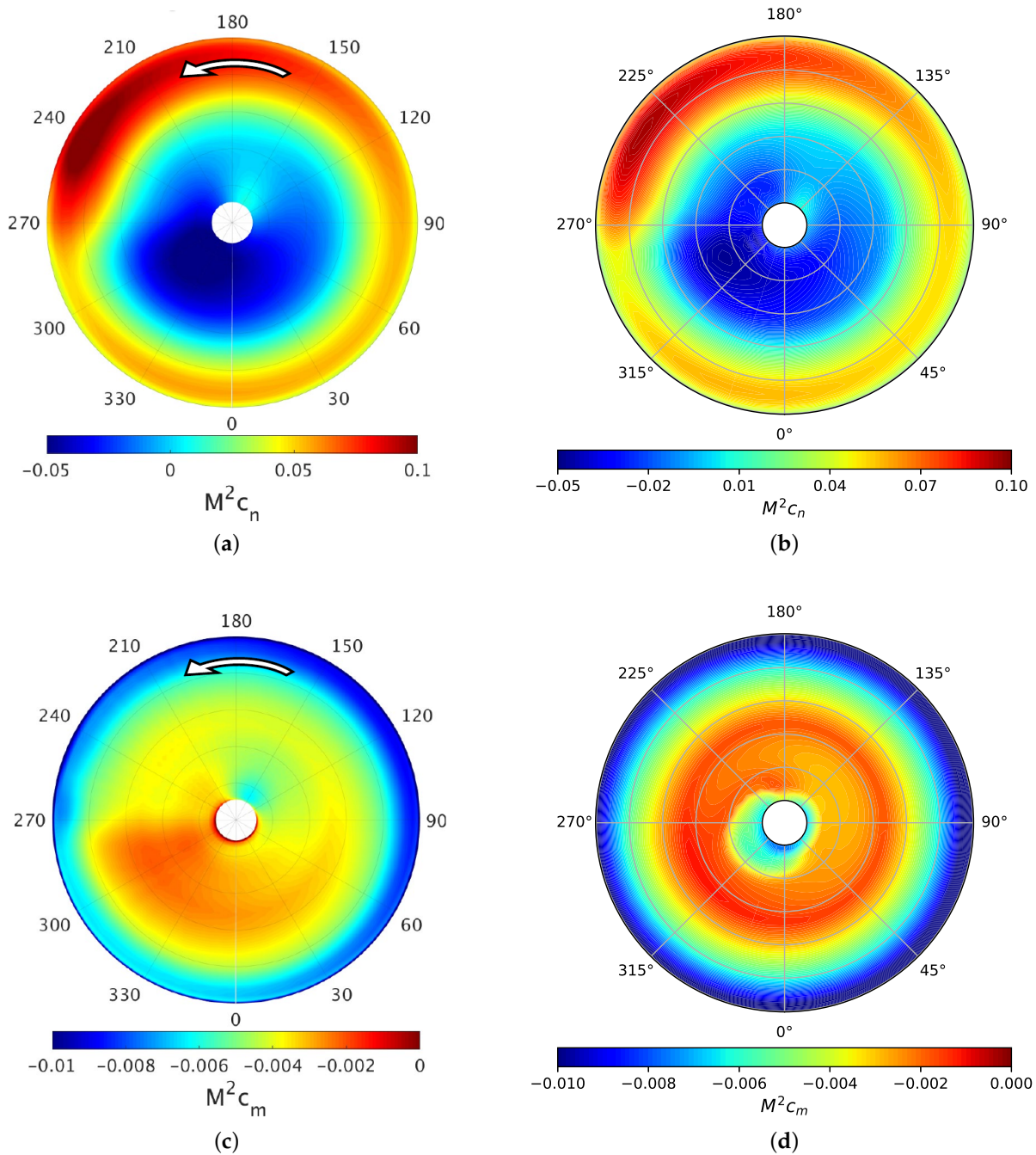
Figure 25. Comparison of the contours of the non-dimensional normal force $M^2 c_n$ and pitching moment $M^2 c_m$ on the proprotor blade in cruise, $\theta_N = 0°$, $V_\infty = 160$ kts, $\Omega = 517$ RPM. (**a**) $M^2 c_n$-CFD [17]; (**b**) $M^2 c_n$-DUST; (**c**) $M^2 c_m$-CFD [17]; (**d**) $M^2 c_m$-DUST.

5. Conclusions

A thorough assessment of the capabilities of a mid-fidelity numerical approach to evaluate the aerodynamic performance and flow physics of a tiltrotor was performed in the present work. Indeed, the results of the numerical simulations performed using the novel mid-fidelity aerodynamic solver DUST based on the vortex particle method were thoroughly compared with the URANS simulation data available in the recent literature for steady flight configurations of the XV-15 tiltrotor aircraft with increasing complexity.

The outcomes of the present work clearly indicate the limits and capabilities of mid-fidelity aerodynamic numerical solvers with respect to the URANS solvers for the evaluation of the aerodynamic performance and interactional flow features of complex VTOL aircraft configurations. In particular, the quite good agreement with the CFD results that were obtained over the different analysed flight conditions indicates that mid-fidelity solvers based on physics-based vortex particle methods are suitable for investigating the main interactional flow features that characterise tiltrotor aerodynamics. The thorough assessment provided in this work opens a novel scenario for aerospace scientific and industrial communities. Indeed, the greatly lower computational effort that is required to run the simulations with respect to CFD indicates that mid-fidelity solvers, such as DUST, represent a valuable tool that can be used in the preliminary design of novel VTOL aircraft architectures, such as tiltrotors, which require a large number of configurations to be investigated to cover the different stages of their flight mission.

Author Contributions: Conceptualisation, A.Z., V.M.; methodology, A.S., M.P., A.Z.; software, A.S., M.T.; validation, A.S., M.P., M.T.; formal analysis, M.P.; investigation, A.S., M.P.; resources, A.S., M.P.; data curation, A.S., M.P., A.Z.; writing—original draft preparation, A.Z.; writing—review and editing, A.Z.; visualisation, A.Z.; supervision, A.Z., V.M.; project administration, A.Z., V.M.; funding acquisition, V.M. All authors have read and agreed to the published version of the manuscript.

Institutional Review Board Statement: Not applicable.

Informed Consent Statement: Not applicable.

Data Availability Statement: The data can be obtained upon request from the corresponding author.

Conflicts of Interest: The authors declare no conflict of interest.

Abbreviations

The following nomenclature and abbreviations are used in this manuscript:

a	speed of sound [m/s]
c	local blade chord
C	blade chord-wise force
CFD	Computational Fluid Dynamics
C_p	pressure coefficient $= \Delta P/(0.5\,\rho R^2\Omega^2)$
C_P	power coefficient $= P/(\rho\pi R^5\Omega^3)$
C_Q	torque coefficient $= Q/(\rho\pi R^5\Omega^2)$
C_T	thrust coefficient $= T/(\rho\pi R^4\Omega^2)$
H	rotor H-force [lbf]
M	blade pitching moment
Mach	freestream Mach number $= V_\infty/a$
M^2C_c	blade sectional chord-wise force coefficient $= C/0.5\,\rho a^2 c$
M^2C_m	blade sectional pitching moment coefficient $= M/0.5\,\rho a^2 c^2$
M^2C_n	blade sectional normal force coefficient $= N/0.5\,\rho a^2 c$
N	blade normal force
N_{rev}	number of rotor revolutions
P	rotor power [hp]
Q	rotor torque [ft-lbf]
r	radial coordinate along the blade
R	rotor radius [m]
T	rotor thrust [lbf]
u	freestream velocity component [m/s]
URANS	Unsteady Reynolds Averaged Navier–Stokes
v	spanwise velocity component [m/s]
V_∞	freestream velocity [m/s]

VPM	vortex particle method
VTOL	vertical takeoff and landing
w	vertical velocity component [m/s]
X	freestream coordinate
Y	spanwise coordinate
Z	vertical coordinate
Z Mach	Mach number based on vertical velocity component $= w/a$
α	wing angle of attack [deg]
α_V	vehicle angle of attack [deg]
ΔP	difference between surface pressure and stagnation pressure
ψ	blade azimuthal angle [deg]
ρ	air density [kg/m^3]
θ	blade pitch angle [deg]
θ_N	nacelle angle [deg]
Ω	rotor speed [RPM]

References

1. Felker, F.F.; Signor, D.B.; Young, L.A.; Betzina, M.D. *Performance and Loads Data from a Hover Test of a 0.658-Scale V-22 Rotor and Wing*; Technical Report TM-89419; NASA: Moffett Field, CA, USA, 1987.
2. Felker, F.F.; Shinoda, P.R.; Heffernan, R.M.; Sheehy, H.F. *Wing Force and Surface Pressure Data from a Hover Test of a 0.658-Scale V-22 Rotor and Wing*; Technical Report TM-102244; NASA: Moffett Field, CA, USA, 1990.
3. Droandi, G.; Gibertini, G.; Grassi, D.; Campanardi, G.; Liprino, C. Proprotor-wing aerodynamic interaction in the first stages of conversion from helicopter to aeroplane mode. *Aerosp. Sci. Technol.* **2016**, *58*, 116–133, doi:10.1016/j.ast.2016.08.013.
4. Droandi, G.; Zanotti, A.; Gibertini, G.; Grassi, D.; Campanardi, G. Experimental investigation of the rotor-wing aerodynamic interaction in a tiltwing aircraft in hover. *Aeronaut. J. New Ser.* **2015**, *119*, 591–612, doi:10.1017/S0001924000010708.
5. Meakin, R. Unsteady Simulation of the Viscous Flow about a V-22 Rotor and Wing in Hover. In Proceedings of the 20th Atmospheric Flight Mechanics Conference 1995, Baltimore, MD, USA, 7–10 August 1995.
6. Potsdam, M.A.; Strawn, R.C. CFD simulations of tiltrotor configurations in hover. *J. Am. Helicopter Soc.* **2005**, *50*, 82–94, doi:10.4050/1.3092845.
7. Wissink, A.; Potsdam, M.; Sankaran, V.; Sitaraman, J.; Yang, Z.; Mavriplis, D. A Coupled Unstructured-Adaptive Cartesian CFD Approach for Hover Prediction. In Proceedings of the American Helicopter Society 66th Annual Forum Proceedings, Phoenix, AZ, USA, 11–13 May 2010.
8. Maisel, M.D.; Giulianetti, D.J.; Dugan, D.C. *The History of the XV-15 Tilt Rotor Research Aircraft: From Concept to Flight*; Number 17; National Aeronautics and Space Administration, Office of Policy and Plans, NASA History Division: Washington, DC, USA, 2000.
9. Cambier, L.; Heib, S.; Plot, S. The Onera elsA CFD software: Input from research and feedback from industry. *Mech. Ind.* **2013**, *14*, 159–174.
10. Kroll, N.; Eisfeld, B.; Bleecke, H. The Navier-Stokes Code FLOWer. *Notes Numer. Fluid Mech.* **1999**, *71*, 58–71.
11. Biava, M.; Woodgate, M.; Barakos, G. Fully implicit discrete-adjoint methods for rotorcraft applications. *AIAA J.* **2016**, *54*, 735–749, doi:10.2514/1.J054006.
12. Biava, M. RANS Computations of Rotor/Fuselage Unsteady Interactional Aerodynamics. Ph.D. Thesis, Politecnico di Milano, Milan, Italy, 2007.
13. Droandi, G.; Zanotti, A.; Gibertini, G. Aerodynamic interaction between rotor and tilting wing in hovering flight condition. *J. Am. Helicopter Soc.* **2015**, *60*, 1–20, doi:10.4050/JAHS.60.042011.
14. Jimenez Garcia, A.; Barakos, G. CFD Simulations on the ERICA Tiltrotor using HMB2. In Proceedings of the 54th AIAA Aerospace Sciences Meeting, San Diego, CA, USA, 4–8 January 2016.
15. Decours, J.; Beaumier, P.; Khier, W.; Kneisch, T.; Valentini, M.; Vigevano, L. Experimental validation of tilt-rotor aerodynamic predictions. In Proceedings of the 40th European Rotorcraft Forum, Southampton, UK, 2–5 September 2014.
16. Tran, S.A.; Lim, J.W. Investigation of the Interactional Aerodynamics of the XV-15 Tiltrotor Aircraft. In Proceedings of the 76th Annual Vertical Flight Society Forum and Technology Display, Virtual, 6–8 October 2020.
17. Tran, S.; Lim, J.; Nunez, G.; Wissink, A.; Bowen-Davies, G. CFD Calculations of the XV-15 tiltrotor during transition. In Proceedings of the American Helicopter Society 75th Annual Forum, Philadelphia, PA, USA, 13–16 May 2019.
18. Lim, J.W. Fundamental Investigation of Proprotor and Wing Interactions in Tiltrotor Aircraft. In Proceedings of the 75th Annual Vertical Flight Society Forum and Technology Display, Philadelphia, PA, USA, 13–16 May 2019.
19. Lim, J.; Tran, S. Interactional Structural Loads of the XV-15 Rotor in Airplane Mode. In Proceedings of the 45th European Rotorcraft Forum, Warsaw, Poland, 17–20 September 2019.

20. Gennaretti, M.; Bernardini, G. Novel Boundary Integral Formulation for Blade–Vortex Interaction Aerodynamics of Helicopter Rotors. *AIAA J.* **2007**, *45*, 1169–1176, doi:10.2514/1.18383.

21. Gennaretti, M.; Molica Colella, M.; Bernardini, G. Prediction of Tiltrotor Vibratory Loads with Inclusion of Wing–Proprotor Aerodynamic Interaction. *J. Aircr.* **2010**, *47*, 71–79, doi:10.2514/1.41825.

22. Wentrup, M.; Yin, J.; Kunze, P.; Streit, T.; Wendisch, J.H.; Schwarz, T.; Pinacho, J.; Kicker, K.; Fukari, R. An overview of DLR compound rotorcraft aerodynamics and aeroacoustics activities within the CleanSky2 NACOR Project. In Proceedings of the 74th AHS Annual Forum & Technology Display, Phoenix, AZ, USA, 14–17 May 2018.

23. Cottet, G.H.; Koumoutsakos, P.D.; Petros, D. *Vortex Methods: Theory and Practice*; Cambridge University Press: Cambridge, UK, 2000.

24. Winckelmans, G.S. Topics in Vortex Methods for the Computation of Three-and Two-Dimensional Incompressible Unsteady Flows. Ph.D. Thesis, California Institute of Technology, Pasadena, CA, USA, 1989.

25. Lu, Y.; Su, T.; Chen, R.; Li, P.; Wang, Y. A method for optimizing the aerodynamic layout of a helicopter that reduces the effects of aerodynamic interaction. *Aerosp. Sci. Technol.* **2019**, *88*, 73–83, doi:10.1016/j.ast.2019.03.005.

26. Opoku, D.; Triantos, D.; Nitzsche, F.; Voutsinas, S. Rotorcraft Aerodynamic and Aeroacoustic Modelling using Vortex Particle Methods. In Proceedings of the 23rd International Congress of Aeronautical Sciences, Toronto, ON, Canada, 8–13 September 2002.

27. Alvarez, E.; Ning, A. Development of a Vortex Particle Code for the Modeling of Wake Interaction in Distributed Propulsion. In Proceedings of the AIAA Applied Aerodynamics Conference, Atlanta, GA, USA, 25–29 June 2018; doi:10.2514/6.2018-3646.

28. Tan, J.; Zhou, T.; Sun, J.; Barakos, G. Numerical investigation of the aerodynamic interaction between a tiltrotor and a tandem rotor during shipboard operations. *Aerosp. Sci. Technol.* **2019**, *87*, 62–72, doi:10.1016/j.ast.2019.02.005.

29. Droandi, G.; Syal, M.; Bower, G. Tiltwing Multi-Rotor Aerodynamic Modeling in Hover, Transition and Cruise Flight Conditions. In Proceedings of the 74th Annual Forum, Phoenix, AZ, USA, 14–17 May 2018.

30. Montagnani, D.; Tugnoli, M.; Zanotti, A.; Syal, M.; Droandi, G. Analysis of the Interactional Aerodynamics of the Vahana eVTOL Using a Medium Fidelity Open Source Tool. In Proceedings of the VFS Aeromechanics for Advanced Vertical Flight Technical Meeting, San Jose, CA, USA, 21–23 January 2020.

31. Piccinini, R.; Tugnoli, M.; Zanotti, A. Numerical Investigation of the Rotor-RotorAerodynamic Interaction for eVTOL Aircraft-Configurations. *Energies* **2020**, *13*, 5995, doi:10.3390/en13225995.

32. Jimenez-Garcia, A.; Barakos, G.; Gates, S. Tiltrotor CFD Part I—validation. *Aeronaut. J.* **2017**, *121*, 577–610, doi:10.1017/aer.2017.17.

33. Morino, L.; Kuot, C.C. Subsonic potential aerodynamics for complex configurations: A general theory. *AIAA J.* **1974**, *12*, 191–197, doi:10.2514/3.49191.

34. Gallay, S.; Laurendeau, E. Nonlinear generalized lifting-line coupling algorithms for pre/poststall flows. *AIAA J.* **2015**, *53*, 1784–1792, doi:10.2514/1.J053530.

35. Piszkin, S.T.; Levinsky, E. *Nonlinear Lifting Line Theory for Predicting Stalling Instabilities on Wings of Moderate Aspect Ratio*; Technical Report, General Dynamics/Convair; National Technical Information Service, San Diego, CA, USA, June 15, 1976.

36. Montagnani, D.; Tugnoli, M.; Fonte, F.; Zanotti, A.; Droandi, G.; Syal, M. Mid-Fidelity Analysis of Unsteady Interactional Aerodynamics of Complex VTOL Configurations. In Proceedings of the 45th European Rotorcraft Forum, Warsaw, Poland, 17–20 September 2019.

37. Brown, R.E.; Line, A.J. Efficient high-resolution wake modeling using the vorticity transport equation. *AIAA J.* **2005**, *43*, 1434–1443, doi:10.2514/1.13679.

38. Lindsay, K.; Krasny, R. A particle method and adaptive treecode for vortex sheet motion in three-dimensional flow. *J. Comput. Phys.* **2001**, *172*, 879–907, doi:10.1006/jcph.2001.6862.

39. Felker, F.F.; Young, L.A.; Signor, D.B. *Performance and Loads Data from a Hover Test of a Full-Scale Advanced Technology XV-15 Rotor*; Technical Memorandum 86854; NASA Ames Research Center: Mountain View, CA, USA, 1986.

40. Bartie, K.; Alexander, H.; McVeigh, M.; Lamon, S.; Bishop, H. *Hover Performance Tests of Baseline Metal and Advanced Technology Blade (ATB) Rotor Systems for the XV-15 Tilt Rotor Aircraft*; Contractor Report 177436; NASA Ames Research Center: Mountain View, CA, USA, 1986.

41. Harris, F.D. H*over Performance of Isolated Proprotors and Propellers-Experimental Data*; Technical Report CR—2017–219486; NASA: Moffett Field, CA, USA, 2017.

42. Bell Helicopter Co. *Advancement of Proprotor Technology Task II: Wind-Tunnel Test Results*; Contractor Report 114363; NASA: Fort Worth, TX, USA, 1971.

43. Drela, M. XFOIL: An Analysis and Design System for Low Reynolds Number Airfoils. In *Low Reynolds Number Aerodynamics*; Mueller, T.J., Ed.; Springer: Berlin/Heidelberg, Germany, 1989; pp. 1–12.

44. Viterna, L.A.; Janetzke, D.C. *Theoretical and Experimental Power from Large Horizontal-Axis Wind Turbines*; Technical Report; Washington Procurement Operations Office: Washington, DC, USA, 1982.

45. Johnson, W. *CAMRAD II, Comprehensive Analytical Model of Rotorcraft Aerodynamics and Dynamics, Volume I: Theory*; Johnson Aeronautics: Johnson Aeronautics, CA, USA, 1992.

46. Ferguson, S.W. *Development and Validation of A Simulation for A Generic Tilt-Rotor Aircraft*; Technical Report CR-166537; NASA: Mountain View, CA, USA, 1989.

47. Palazzi, M. Mid-Fidelity Approach to Tiltrotor Aerodynamics. Master's Thesis, Politecnico di Milano, Milan, Italy, 2020.
48. Arrington, W.; Kumpel, M.; Marr, R. *XV-15 Tilt Rotor Research Aircraft Flight Test Data Report*; Contractor Report 177406; NASA: Washington, DC, USA, 1985.
49. Polak, D.; Rehm, W.; George, A. Effects of an Image Plane on the Tiltrotor Fountain Flow. *J. Am. Helicopter Soc.* **2000**, *45*, 90–96.